

High scale validity of two Higgs doublet scenarios with a real scalar singlet dark matter

Subhaditya Bhattacharya,^a Atri Dey,^b Jayita Lahiri,^c Biswarup Mukhopadhyaya^d

^a*Department of Physics, Indian Institute of Technology Guwahati, North Guwahati, Assam - 781039, India*

^b*School of Theoretical Physics, Dublin Institute for Advanced Studies, 10 Burlington Road, Dublin 4, Ireland*

^c*II. Institut für Theoretische Physik, Universität Hamburg, Luruper Chaussee 149, 22761 Hamburg, Germany*

^d*Department of Physical Sciences, Indian Institute of Science Education and Research Kolkata, Mohanpur - 741246, India*

E-mail: subhab@iitg.ac.in, atri@stp.dias.ie, jayita.lahiri@desy.de, biswarup@iiserkol.ac.in

ABSTRACT: We study the high-scale validity of two kinds of two Higgs doublet models (2HDM), namely, Type-II and Type-X, but with a scalar SU(2) singlet dark matter (DM) candidate in addition in each case. The additional quartic couplings involving the DM particle in the scalar potential in both the scenarios bring in additional constraints from the requirement of perturbative unitarity and vacuum stability. DM relic density and direct search constraints play a crucial role in this analysis as the perturbative unitarity of the DM-Higgs portal couplings primarily decide the high scale validity of the model. We find that, within the parameter regions thus restricted, the Type-II scenario must have a cut-off at around 10^6 GeV, while the Type-X scenario admits of validity upto the Planck scale. However, only those regions which are valid upto about 10^8 GeV in Type-X 2HDM is amenable to detection at the High-luminosity LHC (upto $3000 fb^{-1}$), while most of the parameter space of the Type-II scenario mentioned above is likely to be detectable.

Contents

1	Introduction	2
2	Models and Constraints	3
2.1	Models	3
2.2	Theoretical constraints	4
2.3	Experimental constraints	6
2.4	Dark matter constraints	6
3	Demonstration of running couplings with some benchmarks	7
3.1	The one-loop RGE's	7
3.1.1	Type-II 2HDM	7
3.1.2	Type-X 2HDM	9
3.2	Choice of benchmarks and the running of quartic couplings	10
3.2.1	Type-II 2HDM	11
3.2.2	Type-X 2HDM	13
4	Study of model parameter space	15
4.1	Regions of high-scale validity	15
4.2	Constraints from DM sector	18
4.3	Combining high-scale validity with DM constraints	22
4.4	Prospects at the LHC	23
5	Summary and Conclusions	23
6	Acknowledgements	24
A	Two-loop RGE's	25
A.1	Type-II	25
A.2	Type-X	26

1 Introduction

The discovery and subsequent study of the 125-GeV scalar has almost decisively confirmed the spontaneous breakdown mechanism in the standard electroweak model (SM). It is, however, still possible that more than one scalar SU(2) doublets participate in the electroweak symmetry breaking (EWSB) scheme. Two Higgs doublet models (2HDM) [1] have thus become subjects of frequent investigation, motivated from various unanswered questions in the SM. There are various kinds of 2HDM, for each of which substantial regions of the parameter space are identified as consistent with observed phenomenology. This statement is particularly valid if one remains within the ‘alignment limit’, much of which is accessible to accelerator searches.

Side by side, a question that constantly haunts physicists is the origin of dark matter (DM) in our universe, which strongly suggests physics beyond the SM (BSM), so long as DM is constituted of some yet unknown elementary particle(s). One possibility that is often explored in this context is whether a DM particle, especially a scalar one, can interact with the rest of the SM spectrum through the EWSB sector. Such ‘Higgs portal’ scenarios, however, are strongly constrained from direct DM search data, because of the SM-like scalar contributions to the spin-independent cross-section [2–4]. The restriction, however, become considerably relaxed, if the DM particle has appreciable interaction strength with a heavier neutral scalar in the 2HDM spectrum [5–7]. In that case, not only does one have smaller, propagator-suppressed, contributions to direct search cross-sections, but it is also easier to reduce the tension between the Direct search limits [8, 9] and those from the relic density of the universe [10], due to appropriate interface between more than one contributing channels and the larger number of parameters at one’s disposal. The constraints as well as collider signatures of such *2HDM + scalar DM* scenarios [11–13] have already been explored [5, 7].

We go a step further in the current work. It is a natural question to ask as to what can be the ultraviolet (UV) behaviour of a *2HDM + scalar DM* scenario. Such a question is not only germane in the context of model-building but has also regarding implications in early universe issues, such as electroweak phase transition or the freeze-out of the scalar DM candidate. This issue becomes even more fascinating as the presence of DM turns out to crucially govern the high scale validity of the model.

Keeping such points in mind, we study the high-scale behaviour of such a theoretical scenario. The running of the parameters via Renormalization Group Equations (RGE’s) there lead to additional constraints arising from vacuum stability and perturbative unitarity at high scales. These bring in further restrictions of the allowed regions of the parameter space, over and above the ones already studied. It is thus important to know which parameter regions have chance of revealing themselves at the high-luminosity Large Hadron Collider (HL-LHC), corresponding to different upper limits of validity of this kind of a theory. It is worth mentioning that the high-scale validity of Type-X 2HDM, especially of the parameter space giving rise to the observed anomalous magnetic moment of muon [14–16], has been studied in a previous work [17]. It may be mentioned that the tension between theory and experiment in $g_\mu - 2$ is claimed to have been relaxed on the basis of Lattice calculations [18–21]. We nevertheless have taken a look at the Type-X 2HDM, since it

still allows relatively light (pseudo)scalars, which has a bearing on the evolution of mass parameters upto high-scales. Furthermore, there have been studies on the vacuum stability as well as high scale validity of various other extended scalar sectors, like inert doublets and triplets in association with DM [22–24].

On the whole, the novel features of this study are as follows:

- We take up for our high-scale study two phenomenologically relevant 2HDM types, namely, Type-II (which occurs rather naturally in the supersymmetric SM) and Type-X (which is of interest in the context of muon $(g - 2)$). Each of these scenarios are in addition augmented with one $SU(2)$ singlet DM candidate, for which the scalar potential serves as the portal to SM physics.
- For both these cases, the running of various quartic coupling strengths is studied. A scan is made of the parameter space of each of the scenarios, and the allowed regions the parameter spaces are identified, considering in turn the constraints corresponding to different cut-off scales, and those coming from DM-related issues (mainly direct searches and relic density), in conjunction with the usual phenomenological limits. In particular, the parameter region in Type-X 2HDM improving on the discrepancy in muon $(g - 2)$ is filtered out as an added requirement.
- With the parameter regions thus narrowed down, the potential of capturing the signatures of such scenarios at the HL-LHC are commented upon.

The paper is organized as follows. We discuss the model and theoretical, experimental constraints as well as constraints from the dark matter sector on the model in Section 2. In Section 3, we discuss the RG running of all the couplings and demonstrate with a few benchmark points from Type-II and Type-X 2HDM. We identify the allowed parameters from the perspective of various high-scale validity and dark matter constraints, and discuss the interplay between the two in Section 4. Finally, we summarize and conclude our discussion in Section 5.

2 Models and Constraints

2.1 Models

As stated above, we concentrate on a two Higgs doublet model (2HDM), with an $SU(2)$ real singlet scalar dark matter candidate S . S interacts with two higgs doublets $\Phi_{1,2}$. The scalar potential of the full scenario is

$$\mathcal{V} = \mathcal{V}_{2HDM} + \frac{1}{2}M_S^2 S^2 + \frac{\lambda_S}{4!}S^4 + \lambda_{S1}S^2\Phi_1^\dagger\Phi_1 + \lambda_{S2}S^2\Phi_2^\dagger\Phi_2. \quad (2.1)$$

where the terms in odd powers of S are absent due to a Z_2 symmetry that stabilizes it.

The most general scalar potential involving two scalar doublets in 2HDM is given as follows.

$$\begin{aligned} \mathcal{V}_{2HDM} = & m_{11}^2(\Phi_1^\dagger\Phi_1) + m_{22}^2(\Phi_2^\dagger\Phi_2) - \left[m_{12}^2(\Phi_1^\dagger\Phi_2 + \text{h.c.}) \right] + \frac{\lambda_1}{2}(\Phi_1^\dagger\Phi_1)^2 + \frac{\lambda_2}{2}(\Phi_2^\dagger\Phi_2)^2 \\ & + \lambda_3(\Phi_1^\dagger\Phi_1)(\Phi_2^\dagger\Phi_2) + \lambda_4(\Phi_1^\dagger\Phi_2)(\Phi_2^\dagger\Phi_1) + \left[\frac{\lambda_5}{2}(\Phi_1^\dagger\Phi_2)^2 + \text{h.c.} \right]. \end{aligned} \quad (2.2)$$

We assume CP-conservation, which is ensured by taking all λ_i 's and m_{12}^2 to be real. The two complex Higgs doublets with hypercharge $Y = 1$ can be written as

$$\Phi_1 = \begin{pmatrix} \phi_1^+ \\ \frac{1}{\sqrt{2}}(v_1 + \phi_1^0 + ia_1) \end{pmatrix}, \quad \Phi_2 = \begin{pmatrix} \phi_2^+ \\ \frac{1}{\sqrt{2}}(v_2 + \phi_2^0 + ia_2) \end{pmatrix}. \quad (2.3)$$

Where v_1 and v_2 are the vacuum expectation values of the two doublets, with $v^2 = v_1^2 + v_2^2 = (246 \text{ GeV})^2$ and $\tan\beta = v_2/v_1$. After EWSB, we obtain five physical states, two neutral CP-even scalars, the lighter of which will be called h , and the heavier H , one neutral pseudoscalar A , and a pair of charged scalars H^\pm .

The above potential prevents mixing between S and the scalar doublets as also any vacuum expectation value (VEV) for S . The mass of the DM candidate S is given by, $M_S^{phy^2} = M_S^2 + (\lambda_{S1}v_1^2 + \lambda_{S2}v_2^2)$.

In order to suppress tree-level Flavour changing neutral current (FCNC), one needs to impose further a \mathcal{Z}_2 symmetry in the Yukawa sector. Depending on its nature there are four major Types of 2HDM's. Here we concentrate on Type-II and Type-X 2HDM. In Type-II 2HDM, up-type quarks couple to one doublet, and down-type quarks and charged leptons to the other doublet. Under this assumption, \mathcal{L}_{Yukawa} becomes

$$-\mathcal{L}_{Yukawa} = Y_{u2}\bar{Q}_L\tilde{\Phi}_2u_R + Y_{d1}\bar{Q}_L\Phi_1d_R + Y_{\ell1}\bar{L}_L\Phi_1e_R + \text{h.c.} \quad (2.4)$$

In Type-X 2HDM, on the other hand, the Yukawa interactions are given as

$$-\mathcal{L}_{Yukawa} = Y_{u2}\bar{Q}_L\tilde{\Phi}_2u_R + Y_{d2}\bar{Q}_L\Phi_2d_R + Y_{\ell1}\bar{L}_L\Phi_1e_R + \text{h.c.} \quad (2.5)$$

where Φ_1 couples to leptons only and Φ_2 , only to quarks. In Equation 2.4 and 2.5,

$Q_L^T = (u_L, d_L)$, $L_L^T = (\nu_L, l_L)$, and $\tilde{\Phi}_{1,2} = i\tau_2\Phi_{1,2}^*$. Y_{u2} , Y_{d1}, Y_{d2} and $Y_{\ell1}$ are the couplings of the up, down quarks and leptons with the two doublets where family indices are suppressed.

It should also be noted that \mathcal{Z}_2 symmetry of Yukawa sector is present in the scalar potential as well, excepting for the soft-breaking term m_{12}^2 .

2.2 Theoretical constraints

Theoretical constraints on the model include perturbativity, unitarity and vacuum stability, all the way upto the energy scale which marks the upper limit of validity of the model. Effects of these constraints on various 2HDM parameter spaces have been studied in detail earlier [25–29]. it has been pointed out that large separation between m_A and m_{H^\pm} is disfavored from the requirement of vacuum stability and perturbativity.

• **Vacuum stability:** We would like to check the boundedness from below condition of the scalar potential, which implies there exists no direction in the field space in which $\mathcal{V} \rightarrow -\infty$. This leads to the following conditions on the quartic couplings of the potential [30–32].

$$\lambda_{1,2} > 0, \quad (2.6)$$

$$\lambda_S > 0, \quad (2.7)$$

$$\lambda_3 > -\sqrt{\lambda_1 \lambda_2}, \quad (2.8)$$

$$|\lambda_5| < \lambda_3 + \lambda_4 + \sqrt{\lambda_1 \lambda_2}, \quad (2.9)$$

$$\lambda_{S1} > -\sqrt{\frac{1}{12} \lambda_S \lambda_1}, \lambda_{S2} > -\sqrt{\frac{1}{12} \lambda_S \lambda_2}. \quad (2.10)$$

For negative λ_{S1} or λ_{S2} one additionally has to satisfy,

$$\left(\frac{1}{12} \lambda_S \lambda_1 - \lambda_{S1}^2 \right) > 0, \quad (2.11)$$

$$\left(\frac{1}{12} \lambda_S \lambda_2 - \lambda_{S2}^2 \right) > 0, \quad (2.12)$$

$$-2\lambda_{S1}\lambda_{S2} + \frac{1}{6}\lambda_S\lambda_3 > -\sqrt{4 \left(\frac{1}{12} \lambda_S \lambda_1 - \lambda_{S1}^2 \right) \left(\frac{1}{12} \lambda_S \lambda_2 - \lambda_{S2}^2 \right)}, \quad (2.13)$$

$$-2\lambda_{S1}\lambda_{S2} + \frac{1}{6}\lambda_S(\lambda_3 + \lambda_4 - |\lambda_5|) > -\sqrt{4 \left(\frac{1}{12} \lambda_S \lambda_1 - \lambda_{S1}^2 \right) \left(\frac{1}{12} \lambda_S \lambda_2 - \lambda_{S2}^2 \right)}. \quad (2.14)$$

• **Perturbativity:** If 2HDM is a perturbative quantum field theory at a given scale, it would imply, all quartic couplings, involving the scalar mass eigenstates $C_{H_i H_j H_k H_l} < 4\pi$ and all Yukawa couplings $Y_j < \sqrt{4\pi}$. Further, unitarity bound on the tree level scattering amplitude of the scalars and longitudinal parts of EW gauge bosons put an upper bound on the eigenvalues $|a_i| \leq 8\pi$ of the $2 \rightarrow 2$ scattering matrices [33–38].

The physical masses of the additional scalars can be expressed as:

$$m_A^2 = \frac{m_{12}^2}{\sin \beta \cos \beta} - \lambda_5 v^2, \quad (2.15)$$

$$m_{H^\pm}^2 \approx m_A^2 + \frac{1}{2}v^2(\lambda_5 - \lambda_4). \quad (2.16)$$

It is clear from Equation 2.16 that $m_{H^\pm}^2 - m_A^2$ is proportional to $\lambda_5 - \lambda_4$ which should be less than $\lambda_3 + \sqrt{\lambda_1 \lambda_2}$ from the requirement of boundedness from below (Equation 2.9). Therefore these conditions along with the requirement of perturbativity ie. $C_{H_i H_j H_k H_l} < 4\pi$ puts an upper limit on the mass square difference $m_{H^\pm}^2 - m_A^2$.

The aforementioned constraints can be easily translated into those of the parameter space by expressing the quartic couplings into parameters of the physical basis i.e. masses of the scalars and the mixing angles as follows.

$$\begin{aligned}
\lambda_1 &= \frac{m_H^2 \cos^2 \alpha + m_h^2 \sin^2 \alpha - m_{12}^2 \tan \beta}{v^2 \cos^2 \beta}, \\
\lambda_2 &= \frac{m_H^2 \sin^2 \alpha + m_h^2 \cos^2 \alpha - m_{12}^2 \cot \beta}{v^2 \sin^2 \beta}, \\
\lambda_3 &= \frac{(m_H^2 - m_h^2) \cos \alpha \sin \alpha + 2m_{H^\pm}^2 \sin \beta \cos \beta - m_{12}^2}{v^2 \sin \beta \cos \beta}, \\
\lambda_4 &= \frac{(m_A^2 - 2m_{H^\pm}^2) \sin \beta \cos \beta + m_{12}^2}{v^2 \sin \beta \cos \beta}, \\
\lambda_5 &= \frac{m_{12}^2 - m_A^2 \sin \beta \cos \beta}{v^2 \sin \beta \cos \beta}.
\end{aligned} \tag{2.17}$$

One should note from the expression of λ_1 in Equation 2.17 that, to have it in the perturbative limit, the soft Z_2 breaking parameter $m_{12}^2 \approx \frac{m_H^2}{\tan \beta}$, especially when $m_H \gg m_h$.

2.3 Experimental constraints

Now we briefly discuss experimental constraints on the model parameters.

- **Electroweak Precision measurements:** Electroweak precision measurements [39], especially from the oblique parameters (S, T, U) [40, 41], put significant constraint on 2HDM parameter space when considered at one-loop level, because of the presence of additional scalars. In various earlier works, it is pointed out that the heavier neutral scalar (H) and charged scalar (H^\pm) masses should be closer to each other ($\Delta m \lesssim 50\text{GeV}$), in order to avoid the breaking of custodial $SU(2)$ symmetry [42–46], and at the same time keep the pseudo-scalar mass less constrained. This limit on Δm becomes stronger when H and H^\pm become heavier ($\gtrsim 600\text{GeV}$).

- **Collider bounds:** The CMS and ATLAS data from runs I and II, on the observed SM-like 125-GeV scalar provide measurements of its signal strengths in different channels with increasing precision [47–49]. The data shows significant agreement with the SM predictions of couplings and pushes the limit towards the so-called alignment limit, i.e., $(\beta - \alpha) \approx \frac{\pi}{2}$.

The direct search of non-standard scalars also put severe constraints on the parameter space. For Type-X 2HDM, the $\tau\tau$ final state restricts our parameter space strongly [50, 51], mostly because we choose to work in the low scalar mass and large $\tan \beta$ region, owing its connection to $g_\mu - 2$. For Type-II, on the other hand, the major constraint comes from hh final state [52, 53]. LEP-limits on charged Higgs mass ($\gtrsim 80\text{GeV}$) [54] is imposed for both types. Type-II, in addition, gets constrained from B-physics observables which put a strong lower bound on the charged Higgs mass $m_{H^\pm} \gtrsim 600\text{ GeV}$ [27–29, 55]. All our chosen benchmarks in this work are consistent with the results of `HiggsTools`, in particular, `HiggsSignals` [56–60] and `HiggsBounds` [61–67].

2.4 Dark matter constraints

The WIMP-DM candidate of our model should satisfy the following constraints:

- The thermal relic density should be consistent with the latest Planck data [10].

- The DM-nucleon cross-section must be below the upper bound given by the latest LZ experiment [68].
- Indirect detection constraints of Fermi-LAT experiments coming from isotropic gamma-ray data and the gamma ray observations from dwarf spheroidal galaxies [69] should be satisfied.

3 Demonstration of running couplings with some benchmarks

After discussing all the theoretical and experimental constraints, we examine high-scale validity of such models (*2HDM + scalar*). First we list the RGE's for all gauge, Yukawa and scalar quartic couplings for our model at one-loop level. Though in rest of our work we used two-loop RGE's, we present the Equations for the one-loop RGE's to have an intuitive grasp on the key features of the running of relevant couplings. However, use has been made of the two-loop RGE's [70] only in the subsequent numerical analyses and the results that follow. The two-loop RGE's are shown in detail in Appendix A. We have implemented the model and generated the one and two-loop RG equations in SARAH [71–74]. Subsequently, we evolved the couplings using the aforementioned RG equations using 2HDME [75].

3.1 The one-loop RGE's

We begin by introducing the one-loop RGE's for the gauge couplings. Equation 3.1 demonstrates that they constitute a stand-alone set at one-loop and, as a result, are the same for different types of 2HDM. We would like to mention that GUT normalisation was not used while writing Equation 3.1.

$$\begin{aligned}
16\pi^2\beta_{g_1} &= 7g_1^3, \\
16\pi^2\beta_{g_2} &= -3g_2^3, \\
16\pi^2\beta_{g_3} &= -7g_3^3.
\end{aligned}
\tag{3.1}$$

However, the running of Yukawa couplings as well as quartic couplings pertaining to the scalar sector receive different contribution for different types of 2HDM's since the quark and lepton couplings with the scalar doublets play crucial role in these cases at one-loop level. We present the runnings of the aforementioned couplings for Type-II and Type-X 2HDM's.

3.1.1 Type-II 2HDM

We first concentrate on the RGE of Type-II 2HDM Yukawa couplings. Here, the superscripts g and Y , stand for contributions from the gauge and Yukawa sector, respectively, to the running of the Yukawa couplings (taken here as real).

$$\begin{aligned}
16\pi^2\beta_{Y_t}^g &= -\left(\frac{17}{12}g_1^2 + \frac{9}{4}g_2^2 + 8g_3^2\right)Y_t, \\
16\pi^2\beta_{Y_t}^Y &= \left(\frac{3}{2}Y_b^2 + \frac{9}{2}Y_t^2 + Y_\tau^2\right)Y_t - (Y_b^2 + Y_\tau^2)Y_t, \\
16\pi^2\beta_{Y_b}^g &= -\left(\frac{5}{12}g_1^2 + \frac{9}{4}g_2^2 + 8g_3^2\right)Y_b, \\
16\pi^2\beta_{Y_b}^Y &= \left(\frac{9}{2}Y_b^2 + \frac{3}{2}Y_t^2 + Y_\tau^2\right)Y_b - Y_t^2Y_b, \\
16\pi^2\beta_{Y_\tau}^g &= -\left(\frac{15}{4}g_1^2 + \frac{9}{4}g_2^2\right)Y_\tau, \\
16\pi^2\beta_{Y_\tau}^Y &= \left(\frac{5}{2}Y_\tau^2 + 3Y_b^2\right)Y_\tau.
\end{aligned} \tag{3.2}$$

The resulting beta-function will be the sum of the gauge and Yukawa components.

$$\beta_Y = \beta_Y^g + \beta_Y^Y. \tag{3.3}$$

The relevant equations for the running of quartic couplings are given below. Here, the superscripts b and Y denote, respectively, bosonic(gauge couplings and quartic couplings) and Yukawa interactions, contributing to the running of λ 's.

$$\begin{aligned}
16\pi^2\beta_{\lambda_1}^b &= \frac{3}{4}g_1^4 + \frac{3}{2}g_1^2g_2^2 + \frac{9}{4}g_2^4 - 3g_1^2\lambda_1 - 9g_2^2\lambda_1 + 12\lambda_1^2 + 4\lambda_3^2 + 4\lambda_3\lambda_4 + 2\lambda_4^2 + 2\lambda_5^2 + 4\lambda_{S1}^2, \\
16\pi^2\beta_{\lambda_1}^Y &= -4Y_\tau^4 + 4Y_\tau^2\lambda_1 - 12Y_b^4 + 12Y_b^2\lambda_1, \\
16\pi^2\beta_{\lambda_2}^b &= \frac{3}{4}g_1^4 + \frac{3}{2}g_1^2g_2^2 + \frac{9}{4}g_2^4 - 3g_1^2\lambda_2 - 9g_2^2\lambda_2 + 12\lambda_2^2 + 4\lambda_3^2 + 4\lambda_3\lambda_4 + 2\lambda_4^2 + 2\lambda_5^2 + 4\lambda_{S2}^2, \\
16\pi^2\beta_{\lambda_2}^Y &= -12Y_t^4 + 12Y_t^2\lambda_2, \\
16\pi^2\beta_{\lambda_3}^b &= \frac{3}{4}g_1^4 - \frac{3}{2}g_1^2g_2^2 + \frac{9}{4}g_2^4 - 3g_1^2\lambda_3 - 9g_2^2\lambda_3 + (\lambda_1 + \lambda_2)(6\lambda_3 + 2\lambda_4) + 4\lambda_3^2 + 2\lambda_4^2 + 2\lambda_5^2 + 4\lambda_{S1}\lambda_{S2}, \\
16\pi^2\beta_{\lambda_3}^Y &= (6Y_b^2 + 6Y_t^2 + 2Y_\tau^2)\lambda_3 - 12Y_b^2Y_t^2, \\
16\pi^2\beta_{\lambda_4}^b &= 3g_1^2g_2^2 - (3g_1^2 + 9g_2^2)\lambda_4 + 2\lambda_1\lambda_4 + 2\lambda_2\lambda_4 + 8\lambda_3\lambda_4 + 4\lambda_4^2 + 8\lambda_5^2, \\
16\pi^2\beta_{\lambda_4}^Y &= (6Y_b^2 + 6Y_t^2 + 2Y_\tau^2)\lambda_4 + 12Y_b^2Y_t^2, \\
16\pi^2\beta_{\lambda_5}^b &= (-3g_1^2 - 9g_2^2 + 2\lambda_1 + 2\lambda_2 + 8\lambda_3 + 12\lambda_4)\lambda_5, \\
16\pi^2\beta_{\lambda_5}^Y &= (6Y_b^2 + 6Y_t^2 + 2Y_\tau^2)\lambda_5, \\
16\pi^2\beta_{\lambda_S}^b &= 3(16\lambda_{S1}^2 + 16\lambda_{S2}^2 + \lambda_S^2), \\
16\pi^2\beta_{\lambda_S}^Y &= 0, \\
16\pi^2\beta_{\lambda_{S1}}^b &= -\frac{3}{2}g_1^2\lambda_{S1} - \frac{9}{2}g_2^2\lambda_{S1} + 6\lambda_1\lambda_{S1} + \lambda_S\lambda_{S1} + 4\lambda_3\lambda_{S2} + 2\lambda_4\lambda_{S2} + 8\lambda_{S1}^2, \\
16\pi^2\beta_{\lambda_{S1}}^Y &= 6\lambda_{S1}Y_b^2 + 2\lambda_{S1}Y_\tau^2, \\
16\pi^2\beta_{\lambda_{S2}}^b &= -\frac{3}{2}g_1^2\lambda_{S2} - \frac{9}{2}g_2^2\lambda_{S2} + 6\lambda_2\lambda_{S2} + \lambda_S\lambda_{S2} + 4\lambda_3\lambda_{S1} + 2\lambda_4\lambda_{S1} + 8\lambda_{S2}^2, \\
16\pi^2\beta_{\lambda_{S2}}^Y &= 6\lambda_{S2}Y_t^2.
\end{aligned} \tag{3.4}$$

Like before, the actual beta-function will be the sum of the bosonic and Yukawa components.

$$\beta_\lambda = \beta_\lambda^b + \beta_\lambda^Y. \quad (3.5)$$

Comparing with Equation 2.4, we would like to make the following identifications for type-II 2HDM.

$$Y_{u2} = Y_t, \quad Y_{d1} = Y_b \quad \text{and} \quad Y_{\ell 1} = Y_\tau.$$

3.1.2 Type-X 2HDM

Next we focus on the RGE of the Yukawa couplings in Type-X 2HDM. Here too, the superscripts g and Y stand for contributions from gauge and Yukawa sectors, respectively.

$$\begin{aligned} 16\pi^2 \beta_{Y_t}^g &= - \left(\frac{17}{12} g_1^2 + \frac{9}{4} g_2^2 + 8g_3^2 \right) Y_t, \\ 16\pi^2 \beta_{Y_t}^Y &= \left(\frac{3}{2} Y_b^2 + \frac{9}{2} Y_t^2 \right) Y_t, \\ 16\pi^2 \beta_{Y_b}^g &= - \left(\frac{5}{12} g_1^2 + \frac{9}{4} g_2^2 + 8g_3^2 \right) Y_b, \\ 16\pi^2 \beta_{Y_b}^Y &= \left(\frac{9}{2} Y_b^2 + \frac{3}{2} Y_t^2 \right) Y_b, \\ 16\pi^2 \beta_{Y_\tau}^g &= - \left(\frac{15}{4} g_1^2 + \frac{9}{4} g_2^2 \right) Y_\tau, \\ 16\pi^2 \beta_{Y_\tau}^Y &= \frac{5}{2} Y_\tau^3. \end{aligned} \quad (3.6)$$

The gauge and Yukawa components will be added to provide the final beta-function.

$$\beta_Y = \beta_Y^g + \beta_Y^Y. \quad (3.7)$$

We present next the running of scalar quartic couplings below. The superscripts b and Y bear similar meaning as in the type-II case.

$$\begin{aligned}
16\pi^2\beta_{\lambda_1}^b &= \frac{3}{4}g_1^4 + \frac{3}{2}g_1^2g_2^2 + \frac{9}{4}g_2^4 - 3g_1^2\lambda_1 - 9g_2^2\lambda_1 + 12\lambda_1^2 + 4\lambda_3^2 + 4\lambda_3\lambda_4 + 2\lambda_4^2 + 2\lambda_5^2 + 4\lambda_{S1}^2, \\
16\pi^2\beta_{\lambda_1}^Y &= -4Y_\tau^4 + 4Y_\tau^2\lambda_1, \\
16\pi^2\beta_{\lambda_2}^b &= \frac{3}{4}g_1^4 + \frac{3}{2}g_1^2g_2^2 + \frac{9}{4}g_2^4 - 3g_1^2\lambda_2 - 9g_2^2\lambda_2 + 12\lambda_2^2 + 4\lambda_3^2 + 4\lambda_3\lambda_4 + 2\lambda_4^2 + 2\lambda_5^2 + 4\lambda_{S2}^2, \\
16\pi^2\beta_{\lambda_2}^Y &= -12Y_b^4 - 12Y_t^4 + (12Y_b^2 + 12Y_t^2)\lambda_2, \\
16\pi^2\beta_{\lambda_3}^b &= \frac{3}{4}g_1^4 - \frac{3}{2}g_1^2g_2^2 + \frac{9}{4}g_2^4 - 3g_1^2\lambda_3 - 9g_2^2\lambda_3 + (\lambda_1 + \lambda_2)(6\lambda_3 + 2\lambda_4) + 4\lambda_3^2 + 2\lambda_4^2 + 2\lambda_5^2 + 4\lambda_{S1}\lambda_{S2}, \\
16\pi^2\beta_{\lambda_3}^Y &= (6Y_b^2 + 6Y_t^2 + 2Y_\tau^2)\lambda_3, \\
16\pi^2\beta_{\lambda_4}^b &= 3g_1^2g_2^2 - (3g_1^2 + 9g_2^2)\lambda_4 + 2\lambda_1\lambda_4 + 2\lambda_2\lambda_4 + 8\lambda_3\lambda_4 + 4\lambda_4^2 + 8\lambda_5^2, \\
16\pi^2\beta_{\lambda_4}^Y &= (6Y_b^2 + 6Y_t^2 + 2Y_\tau^2)\lambda_4, \\
16\pi^2\beta_{\lambda_5}^b &= (-3g_1^2 - 9g_2^2 + 2\lambda_1 + 2\lambda_2 + 8\lambda_3 + 12\lambda_4)\lambda_5, \\
16\pi^2\beta_{\lambda_5}^Y &= (6Y_b^2 + 6Y_t^2 + 2Y_\tau^2)\lambda_5, \\
16\pi^2\beta_{\lambda_S}^b &= 3(16\lambda_{S1}^2 + 16\lambda_{S2}^2 + \lambda_S^2), \\
16\pi^2\beta_{\lambda_S}^Y &= 0, \\
16\pi^2\beta_{\lambda_{S1}}^b &= -\frac{3}{2}g_1^2\lambda_{S1} - \frac{9}{2}g_2^2\lambda_{S1} + 6\lambda_1\lambda_{S1} + \lambda_S\lambda_{S1} + 4\lambda_3\lambda_{S2} + 2\lambda_4\lambda_{S2} + 8\lambda_{S1}^2, \\
16\pi^2\beta_{\lambda_{S1}}^Y &= 2\lambda_{S1}Y_\tau^2, \\
16\pi^2\beta_{\lambda_{S2}}^b &= -\frac{3}{2}g_1^2\lambda_{S2} - \frac{9}{2}g_2^2\lambda_{S2} + 6\lambda_2\lambda_{S2} + \lambda_S\lambda_{S2} + 4\lambda_3\lambda_{S1} + 2\lambda_4\lambda_{S1} + 8\lambda_{S2}^2, \\
16\pi^2\beta_{\lambda_{S2}}^Y &= 6\lambda_{S2}Y_t^2 + 6\lambda_{S2}Y_b^2.
\end{aligned} \tag{3.8}$$

The actual beta-function, as before, will be the sum of the bosonic and Yukawa parts.

$$\beta_\lambda = \beta_\lambda^b + \beta_\lambda^Y. \tag{3.9}$$

In case of Type-X 2HDM, comparing with Equation 2.5, we make the following identifications.

$$Y_{u2} = Y_t, \quad Y_{d2} = Y_b \quad \text{and} \quad Y_{\ell1} = Y_\tau.$$

3.2 Choice of benchmarks and the running of quartic couplings

In this subsection we will try to understand the pattern of the running of different quartic couplings for our case. The pattern of running for different 2HDM's are already studied extensively in the literature [17, 70]. Here our main goal is to see how the scalar DM affects the cut-off scales $\Lambda_{UV}^{Cut-off}$, where vacuum stability or unitarity or perturbativity breaks. We would also like to compare this scenario with the 2HDM scenarios. We choose a few different benchmark points, four for each Type-II and Type-X with different values of λ_S , λ_{S1} and λ_{S2} , presented in Table 1 and Table 2 respectively. We show the their running upto their respective cut-off scales $\Lambda_{UV}^{Cut-off}$. Here we use two-loop RGE's of different quartic couplings presented in Appendix A. Please also note that at this stage, the constraints from DM direct search or relic density have not been taken into account. These will come *post facto*, as exemplified in Section 4.

3.2.1 Type-II 2HDM

For Type-II 2HDM benchmark points we choose scalar masses and mixing angles which are allowed by all the theoretical and experimental constraints, as presented below.

$m_h = 125.0$ GeV, $m_H = 588.0$ GeV, $m_A = 588$ GeV, $m_H^\pm = 610$ GeV, $m_{12}^2 = 35776.44128$ GeV²¹, $\tan \beta = 9.6$, $\sin(\beta - \alpha) = 0.998$, which in the general basis leads to $\lambda_1 = 1.60$, $\lambda_2 = 0.21$, $\lambda_3 = 3.15$, $\lambda_4 = 0.42$, $\lambda_5 = 0.03$. Alongside, we choose four sets for DM sector parameters λ_S , λ_{S1} and λ_{S2} (see Table 1).

	Type-II BP1	Type-II BP2	Type-II BP3	Type-II BP4
λ_S	0.0	0.1	1.0×10^{-6}	0.1
λ_{S1}	0.0	0.3	3.0×10^{-6}	2.5
λ_{S2}	0.0	2.0	1.5	2.5
$\Lambda_{UV}^{Cut-off}$ (2-loop) in GeV	5.17×10^3	4.27×10^3	4.79×10^3	1.39×10^3

Table 1. BP's for Type-II 2HDM with singlet scalar DM

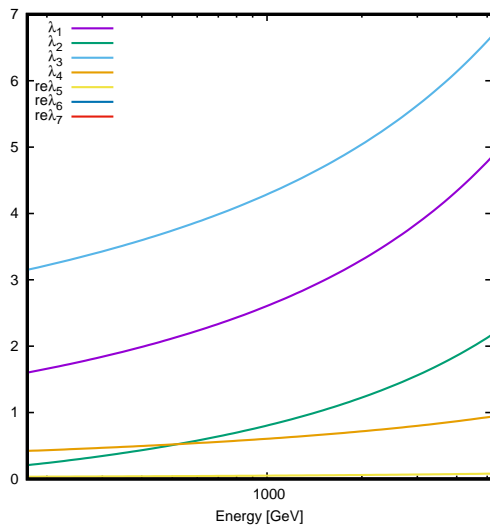
BP1 corresponds to the usual Type-II 2HDM case, without the addition of scalar singlet DM. On the other hand, for BP2 our λ_{S2} is larger than both λ_{S1} and λ_S , which are kept at moderate values. In case of BP3, λ_{S2} is taken to be much larger than λ_S and λ_{S1} , both of which are kept at extremely small values. Finally in BP4, both of the λ_{S1} and λ_{S2} are larger compared to λ_S and λ_S is chosen at a moderate value.

Figure 1 represents the two-loop RG running of various quartic couplings for Type-II scenario with starting scale set at top quark pole mass. In Figure 1(a), λ_S , λ_{S1} and λ_{S2} is set to zero at EW scale. As the RGE's of these three λ 's are always proportional to one of these three λ , all of three remain zero at any energy scale even upto two-loop renormalization. Therefore, in this case the perturbative unitarity of the quartic couplings λ_3 determines the scale of validity.

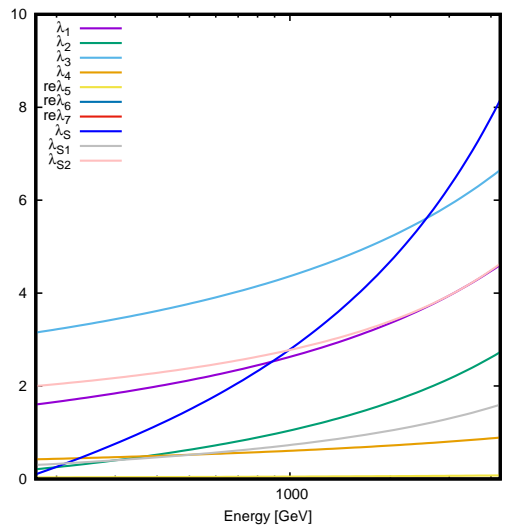
In case of BP2 and BP4, where λ_S has moderate values, the cut-off scale is determined by the perturbativity of λ_S . On the other hand, for BP3, the cut-off scale $\Lambda_{UV}^{Cut-off}$ is determined by the perturbative unitarity of quartic coupling λ_3 , since in this case λ_S is extremely small.

In all the benchmarks in Figure 1, the quartic couplings increase with energy. Since λ_3 is largest among all the quartic couplings at EW scale for our benchmark and its running involves the factor $4\lambda_{S1}\lambda_{S2}$ (see Equation 3.4), its perturbative unitarity breaks at much lower scale for for BP2, BP3 and BP4, compared to BP1 (normal 2HDM), as long as λ_{S1} and λ_{S2} are of the same sign. In such cases, normal 2HDM type-II scenario (BP1) naturally corresponds to largest cut-off scale (see Figure 1(a)). If λ_{S1} and λ_{S2} are of different sign,

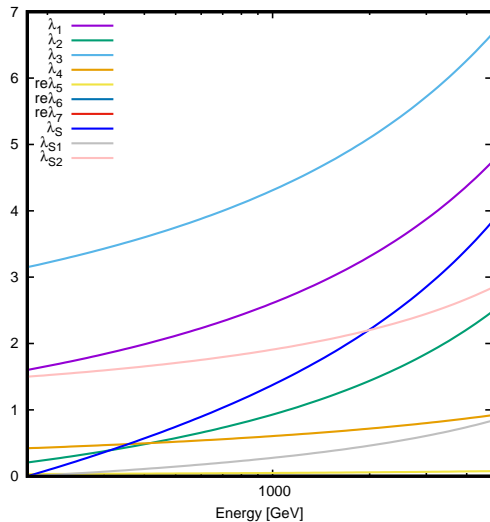
¹Some justification of the places after decimal retained in the various parameters is in order. The parameter m_{12}^2 decides rather sensitively the $m_H - m_h$ splitting and consequently, the scale at which perturbative unitarity breaks. We have noted that a shift in m_{12}^2 by a small amount in decimal places sometimes shifts the cut-off scale by about an order of magnitude. Keeping this in mind, we have retained the values of various parameters upto various decimal places which conform to the results yielded by 2HDM.



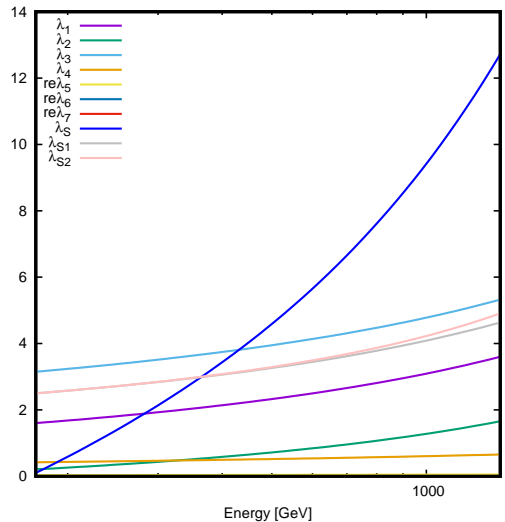
(a) BP1: $\Lambda_{UV}^{Cut-off} = 5.175$ TeV (Unitarity breakdown)



(b) BP2: $\Lambda_{UV}^{Cut-off} = 4.266$ TeV (Unitarity breakdown)



(c) BP3: $\Lambda_{UV}^{Cut-off} = 4.790$ TeV (Unitarity breakdown)



(d) BP4: $\Lambda_{UV}^{Cut-off} = 1.393$ TeV (Perturbativity breakdown)

Figure 1. RG running of quartic couplings for benchmarks (a) BP1, (b) BP2, (c) BP3, (d) BP4 for Type-II with singlet scalar DM scenario. In all cases two-loop RGE's have been used.

the vacuum stability breaks down early on. Therefore even in that case, inclusion of DM worsens the high scale validity of normal 2HDM.

We would like to note that the benchmark points chosen here correspond to a large λ_3 at the EW scale, for which the cut-off scale of the model turns out to be in TeV scale (see Figure 1). However, this is not a generic feature and the model can be valid to much higher scales, as we show in the scan in the next section.

Furthermore, λ_S can also play an important role in the breaking of perturbative uni-

tarity. The running of λ_S is determined by λ_S , λ_{S1} and λ_{S2} . It is therefore clear that for BP4 the perturbativity breaks down at a much lower scale compared to BP2, since the values of λ_{S1} and λ_{S2} for BP4 are largest among all benchmarks.

3.2.2 Type-X 2HDM

For Type-X 2HDM we choose the following benchmarks. Similar to Type-II case, here too, all the masses and mixing angles are allowed by theoretical and experimental constraints, $m_h = 93.6$ GeV, $m_H = 125.0$ GeV, $m_A = 15.8$ GeV, $m_H^\pm = 135.0$, $m_{12}^2 = 393.28757$ GeV²², $\tan\beta = 22.0$ $\sin(\beta - \alpha) = 0.006$. Our chosen masses and mixing angles in the physical basis leads to the following quartic couplings in the flavor basis, $\lambda_1 = 1.03$, $\lambda_2 = 0.26$, $\lambda_3 = 0.59$, $\lambda_4 = -0.45$, $\lambda_5 = 0.14$.

One should note that unlike the Type-II case, here, our SM-like Higgs of 125 GeV mass is the second lightest CP-even scalar, which implies mixing angle $\sin(\beta - \alpha) \ll 1$. This region is favored from the simultaneous requirement of high scale validity and the observed $g_\mu - 2$ [17]. The complementary region where 125 GeV Higgs is the lightest, has been studied in [17] without the inclusion of DM. Note that this is just for illustration; in Section 4, we present a more general parameter scan. Furthermore, we choose four sets for DM sector parameters λ_S , λ_{S1} and λ_{S2} (see Table 2).

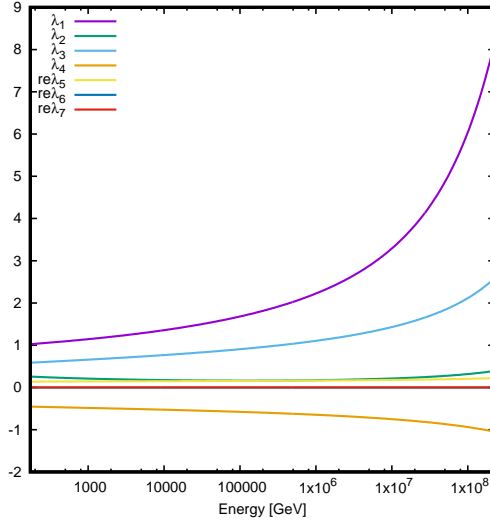
	Type-X BP5	Type-X BP6	Type-X BP7	Type-X BP8
λ_S	0.0	1.0×10^{-6}	1.0×10^{-6}	4.0
λ_{S1}	0.0	0.69	3.0×10^{-6}	-0.24
λ_{S2}	0.0	3.0×10^{-6}	0.69	0.24
$\Lambda_{UV}^{Cut-off}$ (2-loop) in GeV	2.27×10^8	4.49×10^7	2.02×10^8	1.85×10^4

Table 2. BP's for Type-X 2HDM with singlet scalar DM

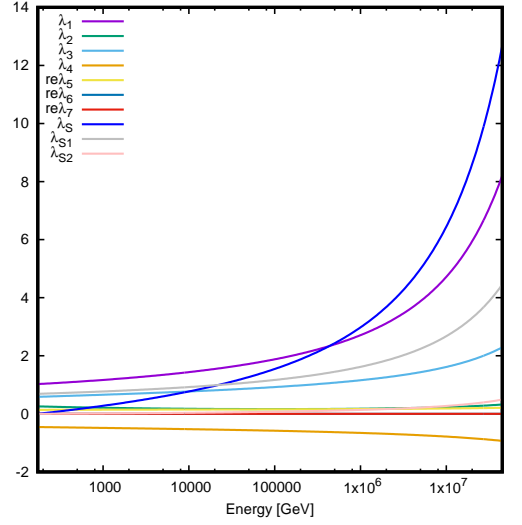
Here too, BP5 represents the usual Type-X 2HDM scenario where the values of new couplings pertaining to DM sector (λ_S , λ_{S1} and λ_{S2}) are set to zero. For BP6, λ_{S1} is chosen to be much larger than the other two couplings, where in BP7 λ_{S2} is much larger than the other two. On the other hand, in BP8, both of the λ_{S1} and λ_{S2} are chosen to be moderate, but smaller compared to λ_S and they have similar magnitude with opposite sign.

Figure 2 represents the one-loop RG evolution of various quartic couplings for Type-X scenario, with the initial scale set at top quark pole mass. In BP5 (Figure 2(a)) λ_S , λ_{S1} and λ_{S2} are set to zero at EW scale and since the RGE's of this three couplings are proportional to at least one of these three couplings (same as Type-II scenario), they remain zero at any higher energy scale for BP5 at one-loop. Therefore, at one-loop level, for BP5 the cut-off scale $\Lambda_{UV}^{Cut-off}$ is determined by the perturbativity and unitarity of quartic couplings of Type-X 2HDM, especially λ_1 , since in our chosen benchmark λ_1 is the largest.

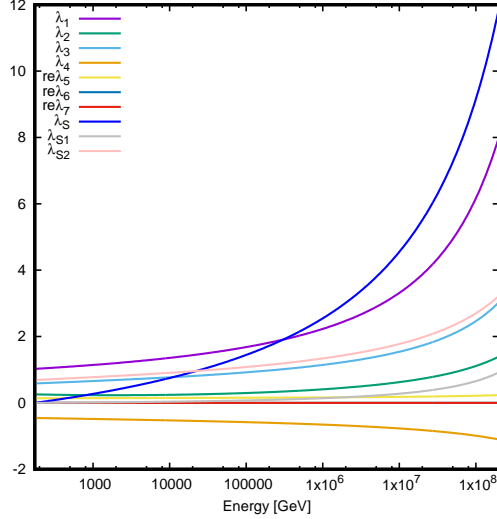
²Here too, the retention of the number of places after decimal for various parameters is guided by the same consideration as that in the case of Type-II 2HDM.



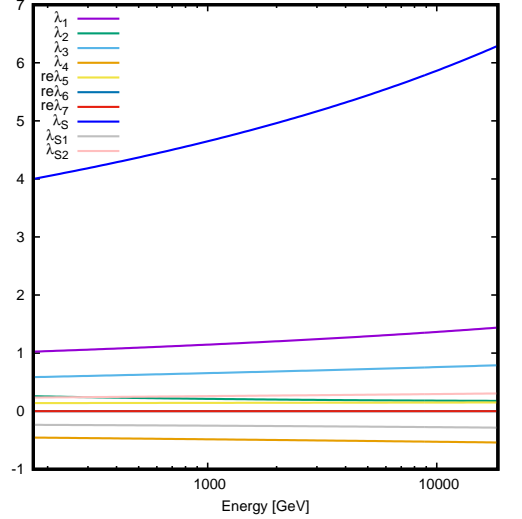
(a) BP5 : $\Lambda_{UV}^{Cut-off} = 2.273 \times 10^5$ TeV (Unitarity breakdown)



(b) BP6 : $\Lambda_{UV}^{Cut-off} = 4.495 \times 10^4$ TeV (Perturbativity breakdown)



(c) BP7 : $\Lambda_{UV}^{Cut-off} = 2.025 \times 10^5$ TeV (Unitarity breakdown)



(d) BP8 : $\Lambda_{UV}^{Cut-off} = 18.49$ TeV (Stability breakdown)

Figure 2. RG running of quartic couplings for the benchmarks (a) BP5, (b) BP6, (c) BP7 and (d) BP8 for Type-X with singlet scalar DM scenario. In all cases two-loop RGE's have been used.

In Figures 2(a), 2(b) and 2(c), all the quartic couplings increase with energy except λ_4 , while in Figure 2(d) both λ_4 and λ_{S1} decrease with energy. λ_1 is largest among all at EW scale for first three benchmarks and its running majorly depends on the factor $4\lambda_{S1}^2$, when λ_{S1}^2 has a non-zero value at EW scale. The perturbative unitarity breaks at a lower scale for BP6 (Figure 2(b)) compared BP7 (Figure 2(c)), because of higher value of λ_{S1} in case of BP6. Similar to Type-II, here too, normal 2HDM Type-X scenario, namely BP5 pertains to the highest cut-off scale. Interestingly, since the running of λ_S is symmetric in

λ_{S1} and λ_{S2} , λ_S runs identically for BP6 and BP7.

On the other hand, λ_S increases much faster than other λ 's for BP8 at two-loop (Figure 2(d)). BP8 shows a distinct behaviour because of the negative sign of λ_{S1} . In this case, the most stringent constraint comes from vacuum stability, if one or both λ_{S1} or λ_{S2} are chosen negative, which breaks the stability at much smaller scale, which is the case with BP8.

In our earlier work [17], we have discussed in detail the running of quartic couplings of Type-X 2HDM. It is not difficult to understand how the presence of the SM-DM and DM-DM couplings affect the allowed parameter space obtained there. We can see from Equations 3.4 and 3.8, λ_1, λ_2 , always gets positive contribution, in terms of $4\lambda_{S1}^2$ and $4\lambda_{S2}^2$ respectively, while λ_3 receives positive or negative contribution ($4\lambda_{S1}\lambda_{S2}$), depending on relative size of λ_{S1} and λ_{S2} . Therefore, if λ_3, λ_{S1} and λ_{S2} are considerably large compared to all other quartic couplings and λ_{S1} and λ_{S2} come with a relative negative sign, there is a possibility of getting a more relaxed parameter space in terms of perturbative unitarity. But in that case, the vacuum stability will be at stake (similar to BP8) and the final allowed parameter space will be more restricted compared to 2HDM parameter space.

It is quite apparent that a WIMP like scalar DM, having sizable portal coupling, restricts the high scale validity of the two Higgs doublet models significantly, while interestingly, a FIMP (Feebly Interacting Massive Particle) like scalar singlet having tiny portal-couplings won't affect the high scale validity of the model so much.

4 Study of model parameter space

4.1 Regions of high-scale validity

After discussing the RG evolutions of all the relevant couplings in the model, we proceed to scan the model parameter space and look for points that satisfy all the theoretical constraints, namely perturbativity, unitarity, and vacuum stability up to cutoff scale $\Lambda_{UV}^{cut-off}$. We have chosen four different scales in this context, namely, $10^4, 10^8, 10^{16}$ and 10^{19} GeV, and present the corresponding allowed regions in the parameter space, spanned by the DM-sector couplings $\lambda_{S1}, \lambda_{S2}$ and λ_S .

In Figure 3 and 4, we show the parameter space valid upto various high-scales in case of Type-II+singlet DM and Type-X+singlet DM scenarios respectively. In any plots, where any two of the three couplings $\lambda_{S1}, \lambda_{S2}$ and λ_S are shown, the third remaining coupling has been varied from -4π to 4π in the scatter plots. Similar marginalization has been carried out for the remaining parameters in the scalar potential.

In Figure 3(a),(b) and (c), we can see that the $\lambda_{S1}, \lambda_{S2} \lesssim 2.0, 0.8, 0.3$ and 0.1 and $\lambda_S \lesssim 6.5, 3.0, 1.5$ and 1 in order for the model to be valid upto 10 TeV, 10^8 GeV, 10^{16} GeV and 10^{20} GeV respectively in Type-II. The results are very similar in case of Type-X as can be seen in Figure 4(a),(b) and (c). In that case, $\lambda_{S1}, \lambda_{S2} \lesssim 2.4, 0.9, 0.4$ and 0.3 and $\lambda_S \lesssim 6.8, 3.2, 1.7$ and 1.2 in order for the model to be valid upto 10 TeV, 10^8 GeV, 10^{16} GeV and 10^{20} GeV respectively.

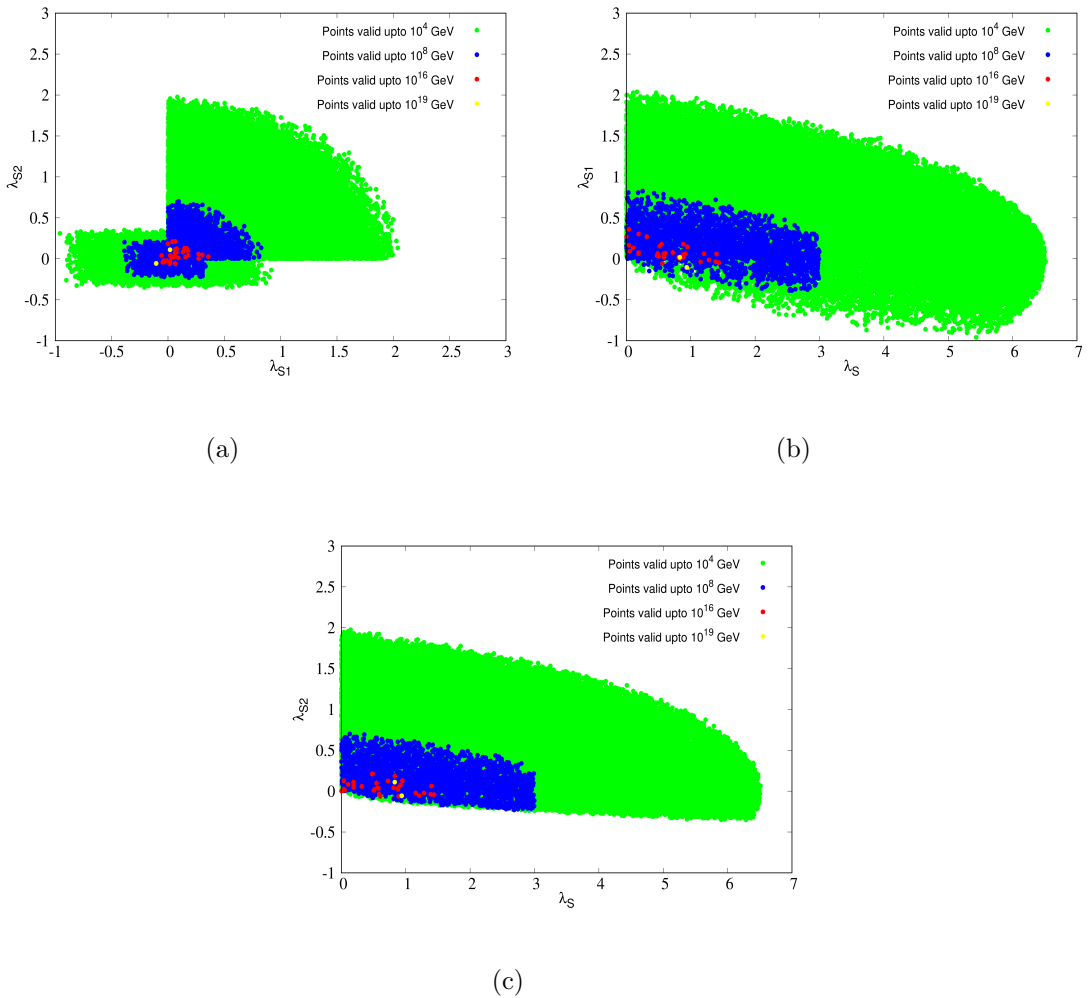


Figure 3. The parameter space spanned by (a) $\lambda_{S1} - \lambda_{S2}$ (b) $\lambda_S - \lambda_{S1}$ and $\lambda_S - \lambda_{S2}$, valid upto different high scales in Type-II 2HDM+DM scenario.

The aforementioned constraints come largely from perturbative unitarity. As we have discussed earlier, the λ_S coupling runs the fastest among all scalar couplings and therefore the perturbativity is driven by λ_S . If we see Equations 3.4 and 3.8, we see that the running of λ_S depends strongly on λ_{S1} as well as λ_{S2} . It is also clear that when λ_{S1} and λ_{S2} are positive, increasing λ_S will imply stronger limits on λ_{S1} as well as λ_{S2} . This is also clear from Figure 3(b),(c) as well as 4(b),(c). In Figures 3 and 4, the regions where either of λ_{S1} and λ_{S2} is negative, get constrained by the requirement of vacuum stability (Equations 2.10) as well.

We would like to point out that, if we compare the regions in Figures 3 and 4, valid upto various scales, we see that the regions follow very similar pattern in Type-II and Type-X, although the Yukawa sectors in both cases are different. The ranges of high scale validity are comparable in both cases, though the allowed region is slightly bigger in Type-X compared to Type-II. We have further checked that, if we are phenomenologically allowed

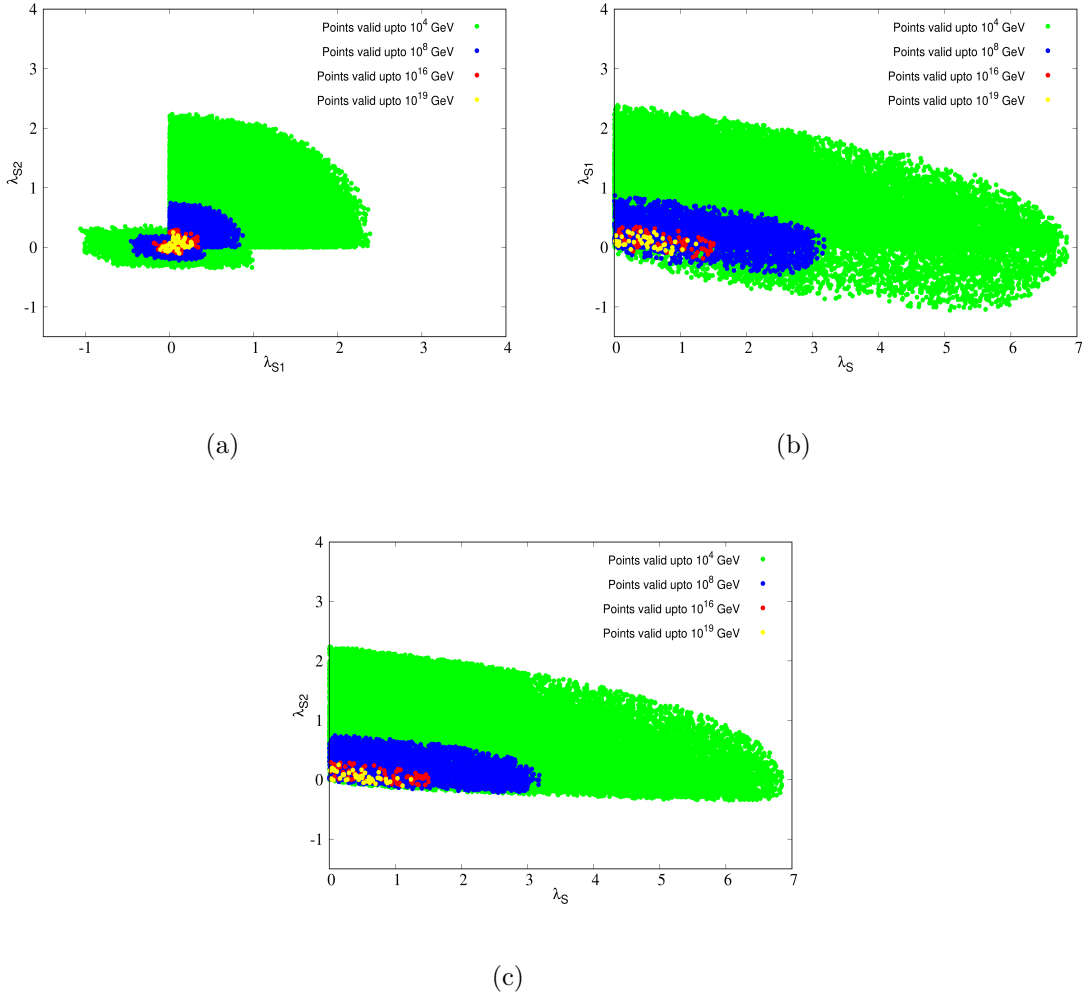


Figure 4. The parameter space spanned by (a) $\lambda_{S1} - \lambda_{S2}$ (b) $\lambda_S - \lambda_{S1}$ and $\lambda_S - \lambda_{S2}$, valid upto different high scales in Type-X 2HDM+DM scenario.

to start with exactly same low-scale values of all the parameters in Type-II and Type-X, the high scale upto which the theories will be valid differs by $\lesssim 100$ GeV. The comparison between the two scenarios in this respect can be summarized as follows:

- As long as λ_S is moderate to large, the perturbativity constraints are strongly driven by λ_S . The running of λ_S has very little contribution from the Yukawa sector, since the Yukawa coupling-dependent terms enter in the running of λ_S , indirectly via λ_{S1} and λ_{S2} . Moreover, Yukawa sector differs for Type-II and Type-X only in terms of Y_b , which is a small quantity compared to the other terms in the running. Therefore, when the λ_S plays dominant role in high-scale validity, little difference is expected between Type-II and Type-X.
- When λ_S is extremely small, the perturbative unitarity is driven by the quartic couplings λ_1 or λ_3 . Although the runnings of these couplings directly involve Yukawa

terms, the smallness of bottom Yukawa ensures that the running remains almost same for Type-II and Type-X.

- We have checked that for the same benchmarks, the limits of high-scale validity differ by $\lesssim 100$ GeV between Type-II and Type-X 2HDM.
- We have further explored the possible difference in the allowed parameter space Type-II and Type-X, after imposing high-scale validity as well as the experimental constraints discussed earlier. This can be seen in terms of the upper limit on λ_{S1} and λ_{S2} . The allowed parameter space is larger for Type-X. The reason is as follows. In Type-X the non-standard scalar masses can be low even after all the collider and B-physics constraints are applied. But in Type-II 2HDM requirements from B-physics as well as collider constraints imply large lower limits on non-standard scalar masses. This in turn necessitates large values of quartic couplings in the EW-scale (see Equations 2.17). Therefore, as a consequence of RG-running the limits on λ_{S1} and λ_{S2} become stronger in case of Type-II as compared to Type-X, following the requirement of perturbative unitarity of the quartic couplings.
- We also see that in the regions allowed upto GUT scale or Planck scale (red and yellow points) in Figures 3 and 4, Type-II case has much fewer points. In the Type-II the heavy scalars have to be much heavier compared to the 125 GeV Higgs (constraint coming from B-physics and collider observables), as can be seen from Equations 2.17. It is therefore extremely difficult to get quartic couplings that are small.

4.2 Constraints from DM sector

An important question arises: which fractions of the parameter regions discussed above are consistent with constraints on a scalar DM? With this in mind, we look next for parameter regions that are allowed by the relic density [10] and direct DM search experiments such as XENON [8, 76, 77], PANDA-X [78, 79] and LUX-ZEPLIN [9]. In this work we have implemented our models in Feynrules [80] and calculated the DM observables with micrOMEGAs [81].

Let us discuss Type-II and Type-X cases one by one. Since DM mass plays an important role in DM-DM annihilation as well as DM-nucleon scattering, we present our results in both cases for three benchmark DM masses, namely $m_{\text{DM}} = 400, 200$ and 62.5 GeV. While implementing the limit from the observed relic density from PLANCK [10], we have made sure that relic density for our parameter points do not exceed the 2σ upper bound. We have also ensured that our DM candidate accounts for at least 10% of the total observed relic, since there is always a possibility that there are multiple DM candidates in nature which can account for the observed relic density collectively. However, we also indicate the regions of parameter space that give rise to the observed relic within 2σ uncertainty.

In Figure 5, we present our results for Type-II 2HDM. Figure 5(a), (b) and (c) represent the allowed parameter space for $m_{\text{DM}} = 400, 200$ and 62.5 GeV respectively, the maroon points satisfy under-relic upto 10%, and the orange points satisfy the upper limit from direct search experiments in addition. The major annihilation channel for the DM pair in

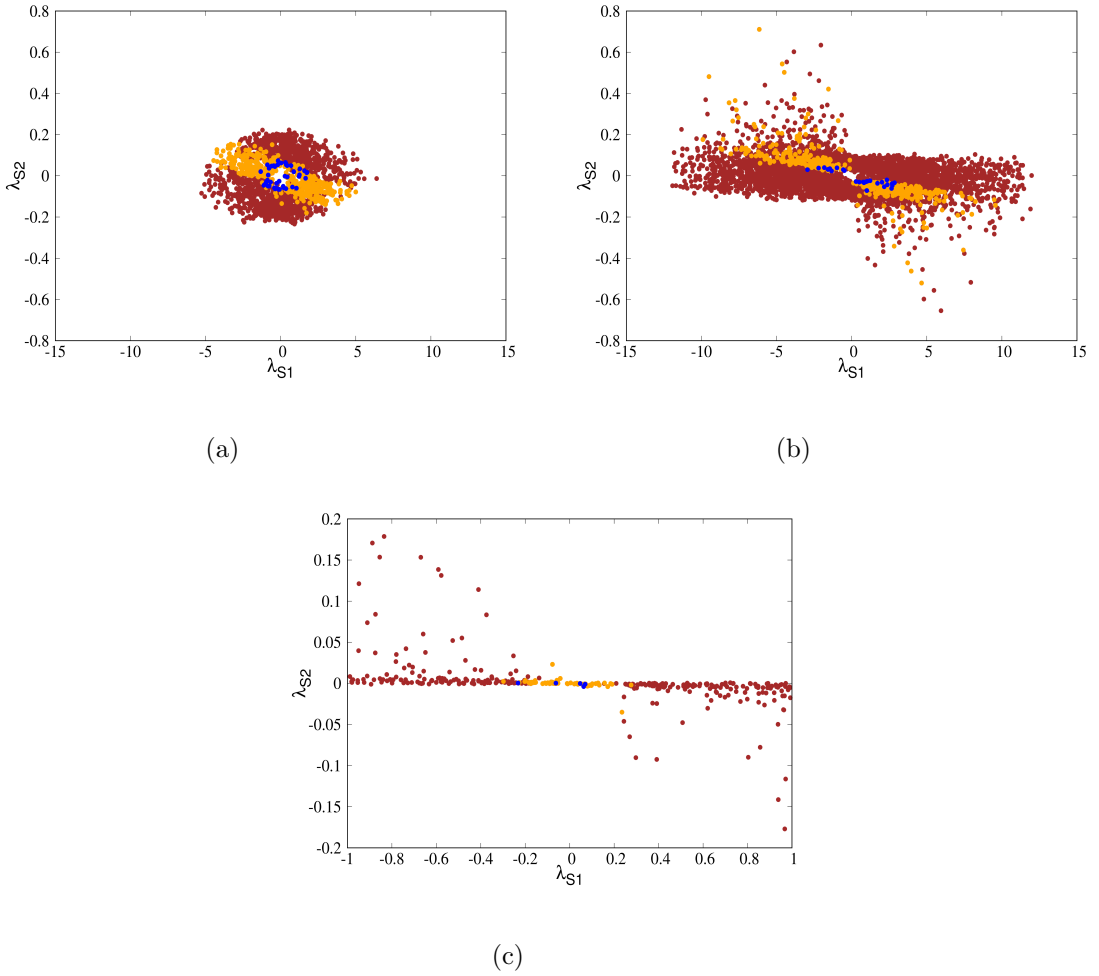


Figure 5. The allowed parameter space in Type-II 2HDM, spanned by $\lambda_{S1}-\lambda_{S2}$ for (a) $m_{DM} = 400$ GeV and (b) $m_{DM} = 200$ GeV and (c) $m_{DM} = 62.5$ GeV. The maroon points have at least 10% contribution to observed relic density, while the orange points satisfy direct detection constraints in addition. The white region at the centre in 5(a) and 5(b) are disallowed by relic over-abundance. The blue points satisfy the actual observed relic density as well as direct detection bound.

this case is into a pair of Higgses. Since in Type-II, the non-standard scalars are heavy $\gtrsim 600$ GeV, the kinematically favored annihilation channel is into SM-Higgs pair, which is typically governed by the λ_{S2} , coupling. Therefore, in all the plots we see the range of λ_{S2} is restricted by the observed relic density to $|\lambda_{S2}| \lesssim 0.2(0.1)$ for 400 GeV (200 GeV) DM mass, whereas the limit on λ_{S1} is more relaxed. However, the limit on λ_{S1} in case of $m_{DM} = 400$ GeV is stronger compared to $m_{DM} = 200$ GeV case. The reason is, for $m_{DM} = 400$ GeV, an additional Hh final state also opens up. Therefore, in this case, the parameter space becomes relic under-abundant with smaller λ_{S1} compared to $m_{DM} = 200$ GeV case. One can see a small region in the center of the $\lambda_{S1} - \lambda_{S2}$ plane, which is disallowed by the relic over-abundance. $|\lambda_{S1}| > 0.9(1)$ for 400 GeV (200 GeV) DM mass.

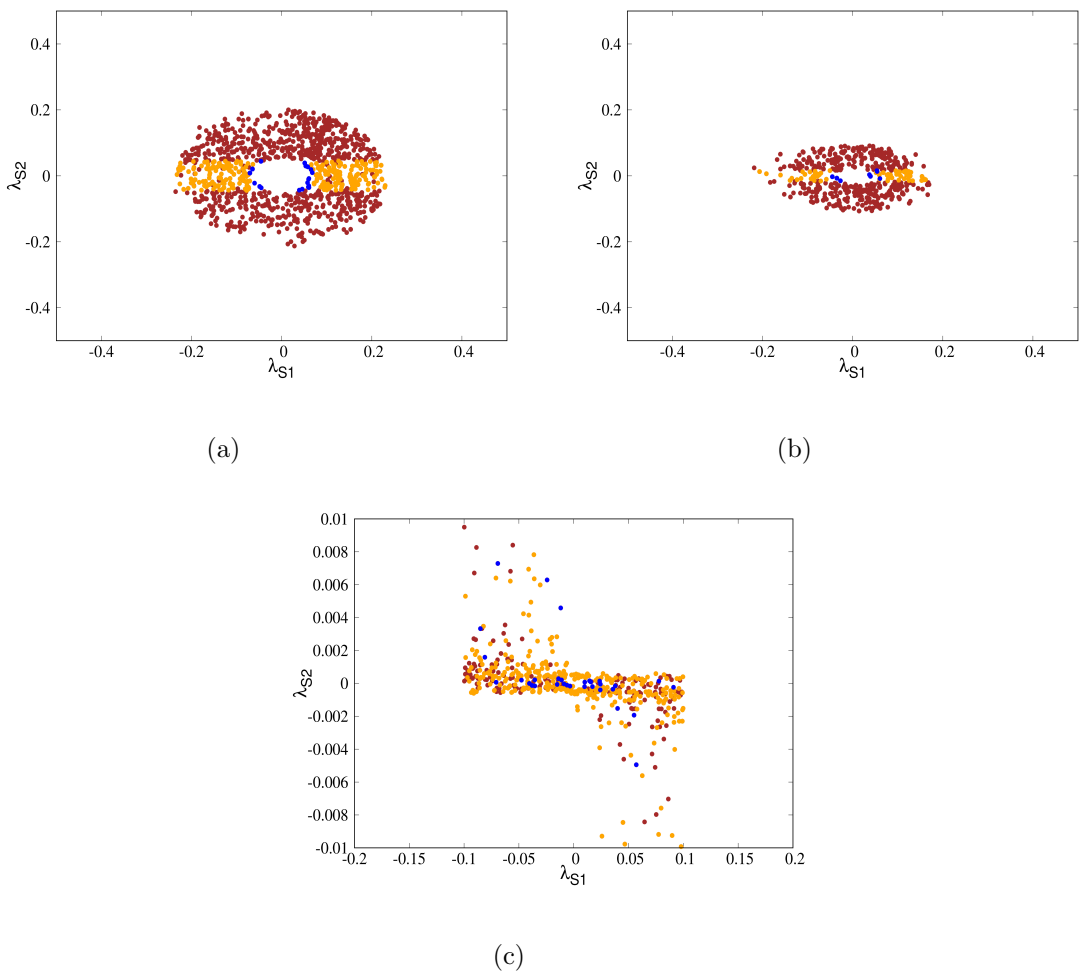


Figure 6. Same as Figure 5, but for Type-X 2HDM.

A special mention is in order for the Higgs-resonance region. Since one of the major annihilation channels for the DM pair is into $b\bar{b}$ final states, the DM mass in the Higgs resonance implies large annihilation cross-section and major under-abundance, unless the relevant coupling λ_{S2} is very small, as can be seen from Figure 5(c). In this region, understandably, the dependence on λ_{S1} is further diminished compared to the other mass points, from the point of view of relic density.

The DM-nucleon elastic scattering cross-section in Type-II 2HDM, shows an interesting pattern in the allowed parameter space. Since the coupling λ_{S2} , which plays a crucial role in the annihilation of DM-pairs, is also responsible for the DM-nucleon scattering, a small DM-nucleon scattering cross-section will necessarily imply small annihilation cross-section and consequently large relic over-abundance. This problem can be avoided in specific regions of the parameter space especially regions of $\tan\beta$, where due to enhanced couplings of the second doublet to down-type quarks in Type-II we can have cancellation between contributions coming from t -channel elastic scatterings involving the two neutral scalars.

This effect was pointed out in [5] earlier. Therefore, in Figure 5, (a) and (b) we see the orange points which are allowed by both observed relic and direct search bound have specific correlation between the two couplings λ_{S1} and λ_{S2} . For $m_{\text{DM}} = 62.5$ GeV i.e. in the vicinity of 125 GeV Higgs resonance, we would get very strong limit on λ_{S2} from relic under-abundance as mentioned earlier, which automatically ensures very small direct search cross-section, as well as $\text{BR}(h_{\text{SM}} \rightarrow \text{invisible}) \lesssim 19\%$ [82]. However, in this case the upper bound from direct search does put a strong limit on $|\lambda_{S1}| \lesssim 0.3$.

In Figures 6, we present the allowed parameter space for the Type-X scenario. Here too, the maroon points satisfy observed relic density (at least 10% of observed relic) and the orange points satisfy the upper bound from direct search experiments in addition. Here too, the preferred annihilation channels are into a pair of scalars. Notably, in Type-X 2HDM, non-standard scalar masses are allowed to be low, therefore annihilation into second non-standard CP-even scalars as well as charged Higgses also takes place. Therefore, we see both λ_{S1} and λ_{S2} become constrained by the observed relic in this case. We can see both $|\lambda_{S1}|$ and $|\lambda_{S2}|$, $\lesssim 0.2(0.15)$ $m_{\text{DM}} = 400(200)$ GeV from relic under-abundance. On the other hand, we see a small region in the middle of the λ_{S1} - λ_{S2} plane disallowed from over-abundance. The corresponding limits on $|\lambda_{S1}|, |\lambda_{S2}| \gtrsim 0.1(0.08)$ for 400 GeV (200 GeV) DM mass. When DM mass is in the vicinity of 125 GeV Higgs resonance, the coupling $|\lambda_{S2}|$ becomes strongly restricted from relic under-abundance, to $\lesssim 0.01$ whereas the other coupling λ_{S1} is naturally less constrained and can vary upto $|\lambda_{S1}| \lesssim 0.1$. One will see the reverse behavior in terms of the two couplings if the DM mass is in the vicinity of resonance of the non-standard scalar.

The region allowed by the direct search experiments shows a very different pattern in Type-X case compared to Type-II 2HDM. Since here the only coupling participating in the DM-nucleon elastic scattering is λ_{S2} (the quarks couple to Φ_2 in this case), the upper bound from direct search experiments only constrains λ_{S2} , while keeping λ_{S1} completely free, as can be seen from Figures 6. When m_{DM} is in the vicinity of Higgs resonance, the smallness of λ_{S2} demanded by relic under-abundance, necessarily ensures small direct search cross-section, similar to Type-II case. However, unlike Type-II, here the direct search bound does not constrain λ_{S1} at all.

One should note that, for our chosen DM mass range of few hundred GeV, the presence of light non-standard scalars make the annihilation process stronger in Type-X model as compared to Type-II. A more restrictive outer contour for Type-X, compared to that in Type-II (see Figures 5 and 6) is a result of demanding at least 10% of the observed relic in both cases. Similarly, the constraint from relic over-abundance affecting the central regions of the plots is more relaxed in Type-X compared to Type-II.

We would like to remind here that the scalar singlet having masses of the order of hundred GeV is still allowed by relic density and direct search constraints having two portal interactions with SM-like and heavy/light Higgs, unlike the usual Higgs-portal scenario, where only SM Higgs portal is present. We also note that while calculating direct search constraints for the relic under-abundant situation (upto 10% contribution), we have been conservative to take the full direct search cross-section, without folding it by the appropriate factor. We have also checked that the parameter space considered here satisfies the

constraints from indirect detection.

4.3 Combining high-scale validity with DM constraints

Having illustrated the regions allowed by perturbative unitarity, vacuum stability upto various high scales, and after studying the regions allowed by DM constraints, namely, observed relic density and direct search, we will confront the two types of constraints with each other. We have seen in Figures 3 and 4 that the high scale validity pushes the DM-portal couplings (λ_{S1} and λ_{S2}) as well as DM self-coupling (λ_S) to smaller values. We have pointed out the upper limits on these couplings, previously. We also point out regions allowed by DM constraints, namely observed relic and direct search. Both these constraints affect only the DM-portal couplings λ_{S1} and λ_{S2} . In Figures 5 and 6, we saw very small couplings are disfavored since they will overclose the universe. Interestingly, this is in tension with the high-scale validity discussed before. In order to examine the contrast between the two, we present a comparison between the two competing constraints in Table 3 for Type-II and 4 for Type-X. We have seen in the previous section that the upper and lower limits on λ_{S1} and λ_{S2} vary a little bit with DM mass. However, it was also evident that the limits from relic over-abundance did not change substantially between 400 GeV and 200 GeV DM mass. Therefore, in order to avoid confusion, we quote only single numbers in the last row Table 3 and 4. Although these numbers can vary slightly with DM mass, our major conclusion remains.

Constraint	Limits on λ_{S1}	Limit on λ_{S2}
High-scale validity upto 10^6 GeV	$\lambda_{S1} \lesssim 1.0$	$\lambda_{S2} \lesssim 1.0$
High-scale validity upto 10^8 GeV	$\lambda_{S1} \lesssim 0.8$	$\lambda_{S2} \lesssim 0.8$
High-scale validity upto 10^{16} GeV	$\lambda_{S1} \lesssim 0.3$	$\lambda_{S2} \lesssim 0.3$
High-scale validity upto 10^{19} GeV	$\lambda_{S1} \lesssim 0.1$	$\lambda_{S2} \lesssim 0.1$
DM constraints	$\lambda_{S1} \gtrsim 1.0$	$\lambda_{S2} \gtrsim 0.1$

Table 3. Type-II: Regions allowed by vacuum stability and perturbative unitarity upto different high scales and regions allowed by DM constraints namely observed relic density as well as direct search of DM. These limits are relaxed in various mass-resonance regions, which is discussed below.

Constraint	Limits on λ_{S1}	Limit on λ_{S2}
High-scale validity upto 10^8 GeV	$\lambda_{S1} \lesssim 0.9$	$\lambda_{S2} \lesssim 0.9$
High-scale validity upto 10^{16} GeV	$\lambda_{S1} \lesssim 0.4$	$\lambda_{S2} \lesssim 0.4$
High-scale validity upto 10^{19} GeV	$\lambda_{S1} \lesssim 0.3$	$\lambda_{S2} \lesssim 0.3$
DM constraints	$\lambda_{S1} \gtrsim 0.1$	$\lambda_{S2} \gtrsim 0.1$

Table 4. Type-X: Regions allowed by vacuum stability and perturbative unitarity upto different high scales and regions allowed by DM constraints namely observed relic density as well as direct search of DM. Similar relaxations as in the Type-II case are also applicable here.

It is clear from the Table 3, that in Type-II+DM scenario, the parameter space can be valid upto $\sim 10^6$ GeV and not higher, in order to remain consistent with the DM constraints. On the other hand, as we see in Table 4, the DM constraints in case of Type-X are less restrictive, and completely satisfy the requirements for validity upto very high scales. To be precise, the entire region of the parameter space consistent with DM constraints is also valid upto the Planck scale in case of Type-X 2HDM in association with a real singlet scalar DM. We would like to highlight this as an important contrast between Type-II and Type-X scenarios in the presence of real singlet scalar DM.

In the discussion and interpretation of Tables 3 and 4, a few comments are in order. The aforementioned limits are strictly valid away from the resonance regions. For example, in Figures 5(c) and 6(c), we see that even with extremely small couplings λ_{S1} and λ_{S2} , the constraints from relic density are satisfied, since the s-channel Higgs-mediated annihilation cross-section is large in this region ($m_{\text{DM}} \approx \frac{m_h}{2}$). Similar relaxation of the relic density constraints occurs when DM-mass is in the vicinity of the CP-even heavy Higgs resonance i.e. $m_{\text{DM}} \approx \frac{m_H}{2}$. In the resonance regions, for both Type-II and Type-X models, DM-constraints allowed parameter spaces can be valid upto the Planck scale.

We also note that the relic density and direct search constraints allow the models to have a cut-off as high as 10^6 GeV or higher, so that the freeze-out of the DM (with $x \sim 20$) is not affected for DM masses upto TeV scale, with dominant depletion contribution coming after EWSB.

4.4 Prospects at the LHC

We briefly comment on the prospect of probing the regions of our models, which are valid upto high scales as well as consistent with DM constraints, at the LHC. In Type-II, we have seen that simultaneous satisfaction of both types of constraints leads to a maximum admissible validity scale 10^6 GeV. The DM-portal couplings λ_{S1} and λ_{S2} are in this case $\gtrsim 1$. In our earlier work [5] we have seen that this region ($\lambda_{S1}, \lambda_{S2} \gtrsim 1$) can be probed at the high-luminosity LHC (3000 fb^{-1}) with $\sim 3\sigma$ significance with cut-based analysis. This happens particularly when a non-standard scalar is produced in vector boson fusion and then decays into a DM pair. It has been shown in that work that the corresponding gluon fusion channel performs rather poorly in this case. Further improvement is possible using machine-learning techniques, as pointed out in [5]. In Type-X, although smaller $\lambda_{S1}, \lambda_{S2}$ couplings are allowed from high-scale validity as well as DM constraints as we pointed out in the previous subsection, there too, at least $\lambda_{S1}, \lambda_{S2} \gtrsim 1$ couplings are required to probe it in the high-luminosity LHC with 3000 fb^{-1} data [7]. Therefore, although the type-X scenario can be valid upto as much as the Planck scale, even after imposing DM constraints, the regions that can be probed at the LHC are restricted to validity limits around 10^8 GeV.

5 Summary and Conclusions

We have explored the high-scale validity in terms of perturbativity, unitarity and vacuum stability, of two-Higgs doublet models with a real singlet scalar DM candidate. Such an

exploration can be expected to yield useful guidelines on scenarios with an extended Higgs sector as the DM portal. In this context, we have considered Type-II 2HDM, which derives its motivation from supersymmetry and Type-X 2HDM, that allows for a low mass pseudo-scalar and provides at least a partial solution to the observed $(g_\mu - 2)$ anomaly. After obtaining the one- and two-loop RG running equations with appropriate modifications/extensions in `SARAH` and `2HDME`, we have identified the differences between the two aforementioned scenarios, in terms of high-scale behavior.

We applied all the experimental constraints on both the models. The B-physics observables as well as direct collider search experiments push the lower limit for non-standard scalars to much higher values in Type-II, as compared to Type-X. The presence of the low mass pseudo-scalars in Type-X 2HDM, not only contributes to $g_\mu - 2$, but also allows for much smaller quartic couplings, at the electro-weak scale, as compared to the Type-II scenario. This in turn, after RG-running, leads to larger allowed regions of parameter space upto various high scales in Type-X case. We have also compared the high-scale validity of 2HDM+DM scenario, with normal 2HDM cases, which was analysed in [17]. We see that the high-scale validity is generally worsened in the presence of a real-singlet DM.

We further study the impact of the high-scale validity on the DM sector. The existing constraints, namely the observed relic density and upper bound from direct search experiments put limits on the portal couplings between DM and the scalar sector. The high scale validity of the model crucially relies on the DM constraints, as the perturbative unitarity of the portal couplings often governs the cut-off scale. In this work, we have identified the regions of parameter space of the aforementioned models, that are allowed by the DM constraints, and are also valid upto various high scales. We find that the Type-II 2HDM+real singlet DM scenario can only be valid upto $\sim 10^6$ GeV from the requirement of perturbative unitarity and vacuum stability, while obeying all the DM constraints at the same time. This implies, such a scenario will require intervention of new physics around $\sim 10^6$ GeV, in order to be viable from the standpoint of particle phenomenology as well as DM-related observations. In Type-X 2HDM + real singlet DM, on the other hand, the restrictions are much more relaxed because of the less stringent phenomenological constraints on the parameter space. It can be valid upto Planck scale while at the same time being allowed by all the existing DM search results. Finally, we comment on the discovery prospect at the high-luminosity LHC, of the regions of the parameter space in these models, that are valid upto high scales, and are also allowed by DM constraints. We find that Type-II 2HDM+real singlet DM, which is valid upto $\sim 10^6$ GeV, can be probed at the high-luminosity LHC. On the other hand, although its Type-X counterpart can be valid upto the Planck scale, only the portion of its parameter space, valid upto $\sim 10^8$ GeV can be probed at the high-luminosity LHC.

6 Acknowledgements

AD and JL would like to thank Indian Institute of Science Education and Research, Kolkata, where part of the work was done.

A Two-loop RGE's

Here we listed the two-loop RGE's of gauge, Yukawa and quartic couplings for our scenario.

A.1 Type-II

$$\begin{aligned}
(16\pi^2\beta_{g_1})_{2-loop} &= (16\pi^2\beta_{g_1})_{2HDM}^{2-loop}, \\
(16\pi^2\beta_{g_2})_{2-loop} &= (16\pi^2\beta_{g_2})_{2HDM}^{2-loop}, \\
(16\pi^2\beta_{g_3})_{2-loop} &= (16\pi^2\beta_{g_3})_{2HDM}^{2-loop}.
\end{aligned} \tag{A.1}$$

The $(16\pi^2\beta_{g_i})_{2HDM}^{2-loop}$, for $i = 1, 2, 3$ represent the RGE's of gauge couplings for general 2HDM's at two-loop level and can be found in [70].

$$\begin{aligned}
(16\pi^2\beta_{Y_t})_{2-loop} &= (16\pi^2\beta_{Y_t})_{2HDM}^{2-loop} + \frac{\lambda_{S_2}^2 Y_t}{16\pi^2}, \\
(16\pi^2\beta_{Y_b})_{2-loop} &= (16\pi^2\beta_{Y_b})_{2HDM}^{2-loop} + \frac{\lambda_{S_1}^2 Y_b}{16\pi^2}, \\
(16\pi^2\beta_{Y_\tau})_{2-loop} &= (16\pi^2\beta_{Y_\tau})_{2HDM}^{2-loop} + \frac{\lambda_{S_1}^2 Y_\tau}{16\pi^2}.
\end{aligned} \tag{A.2}$$

Here too, $(16\pi^2\beta_{Y_j})_{2HDM}^{2-loop}$, where j can be t, b or τ , are the two-loop RGE's for general 2HDM's (can be different for different types). One can easily find out the structure of them from [70]. Next is the RGE's of quartic couplings for our model.

$$\begin{aligned}
(16\pi^2\beta_{\lambda_1})_{2-loop} &= (16\pi^2\beta_{\lambda_1})_{2HDM}^{2-loop} + 4\lambda_{S_1}^2 + \frac{(-32\lambda_{S_1}^3 - 20\lambda_1\lambda_{S_1}^2)}{16\pi^2}, \\
(16\pi^2\beta_{\lambda_2})_{2-loop} &= (16\pi^2\beta_{\lambda_2})_{2HDM}^{2-loop} + 4\lambda_{S_2}^2 + \frac{(-32\lambda_{S_2}^3 - 20\lambda_2\lambda_{S_2}^2)}{16\pi^2}, \\
(16\pi^2\beta_{\lambda_3})_{2-loop} &= (16\pi^2\beta_{\lambda_3})_{2HDM}^{2-loop} + 4\lambda_{S_1}\lambda_{S_2} + \frac{(-16(\lambda_{S_1}^2\lambda_{S_2} + \lambda_{S_2}^2\lambda_{S_1}) - 2\lambda_3(\lambda_{S_1}^2 + \lambda_{S_2}^2 + 8\lambda_{S_1}\lambda_{S_2}))}{16\pi^2}, \\
(16\pi^2\beta_{\lambda_4})_{2-loop} &= (16\pi^2\beta_{\lambda_4})_{2HDM}^{2-loop} + \frac{(-2\lambda_4(\lambda_{S_1}^2 + \lambda_{S_2}^2 + 8\lambda_{S_1}\lambda_{S_2}))}{16\pi^2}, \\
(16\pi^2\beta_{\lambda_5})_{2-loop} &= (16\pi^2\beta_{\lambda_5})_{2HDM}^{2-loop} + \frac{(-2\lambda_5(\lambda_{S_1}^2 + \lambda_{S_2}^2 + 8\lambda_{S_1}\lambda_{S_2}))}{16\pi^2}.
\end{aligned} \tag{A.3}$$

$$\begin{aligned}
(16\pi^2\beta_{\lambda_S})_{2-loop} &= (16\pi^2\beta_{\lambda_S})^{1-loop} + \frac{288}{3}g_1^2(\lambda_{S_1}^2 + \lambda_{S_2}^2) + 288g_2^2(\lambda_{S_1}^2 + \lambda_{S_2}^2) - 384(\lambda_{S_1}^3 + \lambda_{S_2}^3) \\
&\quad - 80\lambda_S(\lambda_{S_1}^2 + \lambda_{S_2}^2) - \frac{17}{3}\lambda_S^3 - 288\lambda_{S_1}^2Y_b^2 - 96\lambda_{S_1}^2Y_\tau^2 - 288\lambda_{S_2}^2Y_t^2, \\
(16\pi^2\beta_{\lambda_{S_1}})_{2-loop} &= (16\pi^2\beta_{\lambda_{S_1}})^{1-loop} + \frac{5}{2}g_1^4\lambda_{S_2} + \frac{15}{2}g_2^4\lambda_{S_2} + \frac{1737}{144}g_1^4\lambda_{S_1} + \frac{15}{8}g_1^2g_2^2\lambda_{S_1} - \frac{123}{16}g_2^4\lambda_{S_1} \\
&\quad - 8\lambda_{S_2}^2\lambda_{S_1} + (12g_1^2 + 36g_2^2)\lambda_2\lambda_{S_1} - 15\lambda_1^2\lambda_{S_1} + (2g_1^2 + 6g_2^2)\lambda_{S_1}^2 - 72\lambda_1\lambda_{S_2}^2 \\
&\quad + (8g_1^2 + 24g_2^2)\lambda_3\lambda_{S_2} - 42\lambda_{S_1}^3 - 16\lambda_3\lambda_{S_2}^2 - 32\lambda_3\lambda_{S_1}\lambda_{S_2} - (8\lambda_{S_2} + 2\lambda_{S_1})\lambda_3^2 \\
&\quad + (4g_1^2 + 12g_2^2)\lambda_4\lambda_{S_2} - 16\lambda_4\lambda_{S_1}\lambda_{S_2} - (8\lambda_{S_2} + 2\lambda_{S_1})\lambda_3\lambda_4 - (8\lambda_{S_2} + 2\lambda_{S_1})\lambda_4^2 - 12\lambda_{S_1}^2\lambda_5 \\
&\quad - (12\lambda_{S_2} - \frac{13}{6}\lambda_{S_1})\lambda_5^2 - 12(2\lambda_3 + \lambda_4)\lambda_{S_1}Y_t^2 - 12\lambda_1\lambda_{S_1}Y_\tau^2 - \frac{9}{2}\lambda_{S_1}Y_b^2Y_t^2 \\
&\quad - (\frac{9}{2}Y_\tau^4 + \frac{27}{2}Y_b^4)\lambda_{S_1} - 8\lambda_{S_1}^2Y_\tau^2 + (\frac{25}{4}g_1^2 + \frac{15}{4}g_2^2)\lambda_{S_1}Y_\tau^2 \\
&\quad + (\frac{25}{12}g_1^2 + \frac{45}{4}g_2^2 + 40g_3^2 - 24\lambda_{S_1} - 36\lambda_1)\lambda_{S_1}Y_b^2, \\
(16\pi^2\beta_{\lambda_{S_2}})_{2-loop} &= (16\pi^2\beta_{\lambda_{S_2}})^{1-loop} + \frac{5}{2}g_1^4\lambda_{S_1} + \frac{15}{2}g_2^4\lambda_{S_1} + \frac{1737}{144}g_1^4\lambda_{S_2} + \frac{15}{8}g_1^2g_2^2\lambda_{S_2} - \frac{123}{16}g_2^4\lambda_{S_2} \\
&\quad - 8\lambda_{S_1}^2\lambda_{S_2} + (12g_1^2 + 36g_2^2)\lambda_2\lambda_{S_2} - 15\lambda_2^2\lambda_{S_2} + (2g_1^2 + 6g_2^2)\lambda_{S_2}^2 - 72\lambda_2\lambda_{S_2}^2 \\
&\quad + (8g_1^2 + 24g_2^2)\lambda_3\lambda_{S_1} - 42\lambda_{S_2}^3 - 16\lambda_3\lambda_{S_1}^2 - 32\lambda_3\lambda_{S_1}\lambda_{S_2} - (8\lambda_{S_1} + 2\lambda_{S_2})\lambda_3^2 \\
&\quad + (4g_1^2 + 12g_2^2)\lambda_4\lambda_{S_1} - 16\lambda_4\lambda_{S_1}\lambda_{S_2} - (8\lambda_{S_1} + 2\lambda_{S_2})\lambda_3\lambda_4 - (8\lambda_{S_1} + 2\lambda_{S_2})\lambda_4^2 - 12\lambda_{S_2}^2\lambda_5 \\
&\quad - (12\lambda_{S_1} - \frac{13}{6}\lambda_{S_2})\lambda_5^2 - 12(2\lambda_3 + \lambda_4)\lambda_{S_1}Y_b^2 - (8\lambda_3 + 4\lambda_4)\lambda_{S_1}Y_\tau^2 - \frac{9}{2}\lambda_{S_2}Y_b^2Y_t^2 - \frac{27}{2}\lambda_{S_2}Y_t^4 \\
&\quad + (\frac{85}{12}g_1^2 + \frac{45}{4}g_2^2 + 40g_3^2 - 24\lambda_{S_2} - 36\lambda_2)\lambda_{S_2}Y_t^2. \tag{A.4}
\end{aligned}$$

A.2 Type-X

$$\begin{aligned}
(16\pi^2\beta_{g_1})_{2-loop} &= (16\pi^2\beta_{g_1})_{2HDM}^{2-loop}, \\
(16\pi^2\beta_{g_2})_{2-loop} &= (16\pi^2\beta_{g_2})_{2HDM}^{2-loop}, \\
(16\pi^2\beta_{g_3})_{2-loop} &= (16\pi^2\beta_{g_3})_{2HDM}^{2-loop}. \tag{A.5}
\end{aligned}$$

The $(16\pi^2\beta_{g_i})_{2HDM}^{2-loop}$, for $i = 1, 2, 3$ represent the RGE's of gauge couplings for general 2HDM's at two-loop level and can be found in [70].

$$\begin{aligned}
(16\pi^2\beta_{Y_t})_{2-loop} &= (16\pi^2\beta_{Y_t})_{2HDM}^{2-loop} + \frac{\lambda_{S_2}^2 Y_t}{16\pi^2}, \\
(16\pi^2\beta_{Y_b})_{2-loop} &= (16\pi^2\beta_{Y_b})_{2HDM}^{2-loop} + \frac{\lambda_{S_2}^2 Y_b}{16\pi^2}, \\
(16\pi^2\beta_{Y_\tau})_{2-loop} &= (16\pi^2\beta_{Y_\tau})_{2HDM}^{2-loop} + \frac{\lambda_{S_1}^2 Y_\tau}{16\pi^2}. \tag{A.6}
\end{aligned}$$

Here too, $(16\pi^2\beta_{Y_j})_{2HDM}^{2-loop}$, where j can be t, b or τ , are the two-loop RGE's for general 2HDM's (can be different for different types). One can easily find out the structure of them

from [70]. Next is the RGE's of quartic couplings for our model.

$$\begin{aligned}
(16\pi^2\beta_{\lambda_1})_{2-loop} &= (16\pi^2\beta_{\lambda_1})_{2HDM}^{2-loop} + 4\lambda_{S1}^2 + \frac{(-32\lambda_{S1}^3 - 20\lambda_1\lambda_{S1}^2)}{16\pi^2}, \\
(16\pi^2\beta_{\lambda_2})_{2-loop} &= (16\pi^2\beta_{\lambda_2})_{2HDM}^{2-loop} + 4\lambda_{S2}^2 + \frac{(-32\lambda_{S2}^3 - 20\lambda_2\lambda_{S2}^2)}{16\pi^2}, \\
(16\pi^2\beta_{\lambda_3})_{2-loop} &= (16\pi^2\beta_{\lambda_3})_{2HDM}^{2-loop} + 4\lambda_{S1}\lambda_{S2} + \frac{(-16(\lambda_{S1}^2\lambda_{S2} + \lambda_{S2}^2\lambda_{S1}) - 2\lambda_3(\lambda_{S1}^2 + \lambda_{S2}^2 + 8\lambda_{S1}\lambda_{S2}))}{16\pi^2}, \\
(16\pi^2\beta_{\lambda_4})_{2-loop} &= (16\pi^2\beta_{\lambda_4})_{2HDM}^{2-loop} + \frac{(-2\lambda_4(\lambda_{S1}^2 + \lambda_{S2}^2 + 8\lambda_{S1}\lambda_{S2}))}{16\pi^2}, \\
(16\pi^2\beta_{\lambda_5})_{2-loop} &= (16\pi^2\beta_{\lambda_5})_{2HDM}^{2-loop} + \frac{(-2\lambda_5(\lambda_{S1}^2 + \lambda_{S2}^2 + 8\lambda_{S1}\lambda_{S2}))}{16\pi^2}. \tag{A.7}
\end{aligned}$$

$$\begin{aligned}
(16\pi^2\beta_{\lambda_S})_{2-loop} &= (16\pi^2\beta_{\lambda_S})^{1-loop} + \frac{288}{3}g_1^2(\lambda_{S1}^2 + \lambda_{S2}^2) + 288g_2^2(\lambda_{S1}^2 + \lambda_{S2}^2) - 384(\lambda_{S1}^3 + \lambda_{S2}^3) \\
&\quad - 80\lambda_S(\lambda_{S1}^2 + \lambda_{S2}^2) - \frac{17}{3}\lambda_S^3 - 288\lambda_{S2}^2Y_b^2 - 96\lambda_{S1}^2Y_\tau^2 - 288\lambda_{S2}^2Y_t^2, \\
(16\pi^2\beta_{\lambda_{S1}})_{2-loop} &= (16\pi^2\beta_{\lambda_{S1}})^{1-loop} + \frac{5}{2}g_1^4\lambda_{S2} + \frac{15}{2}g_2^4\lambda_{S2} + \frac{1737}{144}g_1^4\lambda_{S1} + \frac{15}{8}g_1^2g_2^2\lambda_{S1} - \frac{123}{16}g_2^4\lambda_{S1} \\
&\quad - 8\lambda_{S2}^2\lambda_{S1} + (12g_1^2 + 36g_2^2)\lambda_2\lambda_{S1} - 15\lambda_1^2\lambda_{S1} + (2g_1^2 + 6g_2^2)\lambda_{S1}^2 - 72\lambda_1\lambda_{S2}^2 \\
&\quad + (8g_1^2 + 24g_2^2)\lambda_3\lambda_{S2} - 42\lambda_{S1}^3 - 16\lambda_3\lambda_{S2}^2 - 32\lambda_3\lambda_{S1}\lambda_{S2} - (8\lambda_{S2} + 2\lambda_{S1})\lambda_3^2 \\
&\quad + (4g_1^2 + 12g_2^2)\lambda_4\lambda_{S2} - 16\lambda_4\lambda_{S1}\lambda_{S2} - (8\lambda_{S2} + 2\lambda_{S1})\lambda_3\lambda_4 - (8\lambda_{S2} + 2\lambda_{S1})\lambda_4^2 - 12\lambda_{S1}^2\lambda_5 \\
&\quad - (12\lambda_{S2} - \frac{13}{6}\lambda_{S1})\lambda_5^2 - 12(2\lambda_3 + \lambda_4)\lambda_{S2}(Y_t^2 + Y_b^2) - 12\lambda_1\lambda_{S1}Y_\tau^2 - \frac{9}{2}Y_\tau^4\lambda_{S1} - 8\lambda_{S1}^2Y_\tau^2 \\
&\quad + (\frac{25}{4}g_1^2 + \frac{15}{4}g_2^2)\lambda_{S1}Y_\tau^2, \\
(16\pi^2\beta_{\lambda_{S2}})_{2-loop} &= (16\pi^2\beta_{\lambda_{S2}})^{1-loop} + \frac{5}{2}g_1^4\lambda_{S1} + \frac{15}{2}g_2^4\lambda_{S1} + \frac{1737}{144}g_1^4\lambda_{S2} + \frac{15}{8}g_1^2g_2^2\lambda_{S2} - \frac{123}{16}g_2^4\lambda_{S2} \\
&\quad - 8\lambda_{S1}^2\lambda_{S2} + (12g_1^2 + 36g_2^2)\lambda_2\lambda_{S2} - 15\lambda_2^2\lambda_{S2} + (2g_1^2 + 6g_2^2)\lambda_{S2}^2 - 72\lambda_2\lambda_{S2}^2 \\
&\quad + (8g_1^2 + 24g_2^2)\lambda_3\lambda_{S1} - 42\lambda_{S2}^3 - 16\lambda_3\lambda_{S1}^2 - 32\lambda_3\lambda_{S1}\lambda_{S2} - (8\lambda_{S1} + 2\lambda_{S2})\lambda_3^2 \\
&\quad + (4g_1^2 + 12g_2^2)\lambda_4\lambda_{S1} - 16\lambda_4\lambda_{S1}\lambda_{S2} - (8\lambda_{S1} + 2\lambda_{S2})\lambda_3\lambda_4 - (8\lambda_{S1} + 2\lambda_{S2})\lambda_4^2 - 12\lambda_{S2}^2\lambda_5 \\
&\quad - (12\lambda_{S1} - \frac{13}{6}\lambda_{S2})\lambda_5^2 - 4(2\lambda_3 + \lambda_4)\lambda_{S1}Y_\tau^2 - \frac{272}{3}(Y_t^4 + Y_b^4)\lambda_{S2} - 21\lambda_{S2}Y_b^2Y_t^2 \\
&\quad - (36\lambda_2 + 24\lambda_{S2})\lambda_{S2}Y_t^2 + (\frac{25}{12}g_1^2 + \frac{45}{4}g_2^2 + 40g_3^2 - 24\lambda_{S2} - 36\lambda_2)\lambda_{S2}Y_b^2 \\
&\quad + (\frac{85}{12}g_1^2 + \frac{45}{4}g_2^2 + 40g_3^2)\lambda_{S2}Y_t^2. \tag{A.8}
\end{aligned}$$

In the case of the usual quartic couplings present in general 2HDM's, which are $\lambda_{1,..,5}$, we use the term $(16\pi^2\beta_{\lambda_k})_{2HDM}^{2-loop}$ ($k = 1, ..5$) to represent the two-loop RGE's of respective couplings at two-loop in general 2HDM model for different types (see [70]). On the other hand, for the other three quartic couplings, namely λ_S , λ_{S1} and λ_{S2} , the terms, $(16\pi^2\beta_{\lambda_l})^{1-loop}$ ($l = S, S1$ or $S2$) represent the one-loop RGE's of respective coupling for our case for Type-II and Type-X 2HDM respectively.

References

- [1] G. C. Branco, P. M. Ferreira, L. Lavoura, M. N. Rebelo, M. Sher and J. P. Silva, *Theory and phenomenology of two-Higgs-doublet models*, *Phys. Rept.* **516** (2012) 1–102, [[1106.0034](#)].
- [2] L. Lopez-Honorez, T. Schwetz and J. Zupan, *Higgs portal, fermionic dark matter, and a Standard Model like Higgs at 125 GeV*, *Phys. Lett. B* **716** (2012) 179–185, [[1203.2064](#)].
- [3] A. Greljo, J. Julio, J. F. Kamenik, C. Smith and J. Zupan, *Constraining Higgs mediated dark matter interactions*, *JHEP* **11** (2013) 190, [[1309.3561](#)].
- [4] M. A. Fedderke, J.-Y. Chen, E. W. Kolb and L.-T. Wang, *The Fermionic Dark Matter Higgs Portal: an effective field theory approach*, *JHEP* **08** (2014) 122, [[1404.2283](#)].
- [5] A. Dey, J. Lahiri and B. Mukhopadhyaya, *LHC signals of a heavy doublet Higgs as dark matter portal: cut-based approach and improvement with gradient boosting and neural networks*, *JHEP* **09** (2019) 004, [[1905.02242](#)].
- [6] A. Dey, J. Lahiri and B. Mukhopadhyaya, *LHC signals of triplet scalars as dark matter portal: cut-based approach and improvement with gradient boosting and neural networks*, *JHEP* **06** (2020) 126, [[2001.09349](#)].
- [7] A. Dey and J. Lahiri, *Collider Signatures of Type-X 2HDM + scalar singlet dark matter at HL-LHC*, [2112.15536](#).
- [8] XENON collaboration, E. Aprile et al., *Dark Matter Search Results from a One Ton-Year Exposure of XENON1T*, *Phys. Rev. Lett.* **121** (2018) 111302, [[1805.12562](#)].
- [9] LZ collaboration, J. Aalbers et al., *First Dark Matter Search Results from the LUX-ZEPLIN (LZ) Experiment*, [2207.03764](#).
- [10] PLANCK collaboration, N. Aghanim et al., *Planck 2018 results. VI. Cosmological parameters*, *Astron. Astrophys.* **641** (2020) A6, [[1807.06209](#)].
- [11] A. Drozd, B. Grzadkowski, J. F. Gunion and Y. Jiang, *Extending two-Higgs-doublet models by a singlet scalar field - the Case for Dark Matter*, *JHEP* **11** (2014) 105, [[1408.2106](#)].
- [12] M. Muhlleitner, M. O. P. Sampaio, R. Santos and J. Wittbrodt, *The N2HDM under Theoretical and Experimental Scrutiny*, *JHEP* **03** (2017) 094, [[1612.01309](#)].
- [13] I. Engeln, P. Ferreira, M. M. Muhlleitner, R. Santos and J. Wittbrodt, *The Dark Phases of the N2HDM*, *JHEP* **08** (2020) 085, [[2004.05382](#)].
- [14] MUON G-2 collaboration, G. W. Bennett et al., *Final Report of the Muon E821 Anomalous Magnetic Moment Measurement at BNL*, *Phys. Rev.* **D73** (2006) 072003, [[hep-ex/0602035](#)].
- [15] MUON G-2 collaboration, B. Abi et al., *Measurement of the Positive Muon Anomalous Magnetic Moment to 0.46 ppm*, *Phys. Rev. Lett.* **126** (2021) 141801, [[2104.03281](#)].
- [16] MUON G-2 collaboration, T. Albahri et al., *Measurement of the anomalous precession frequency of the muon in the Fermilab Muon g – 2 Experiment*, *Phys. Rev.* **D103** (2021) 072002, [[2104.03247](#)].
- [17] A. Dey, J. Lahiri and B. Mukhopadhyaya, *Muon g-2 and a type-X two-Higgs-doublet scenario: Some studies in high-scale validity*, *Phys. Rev. D* **106** (2022) 055023, [[2106.01449](#)].
- [18] S. Borsanyi et al., *Leading hadronic contribution to the muon magnetic moment from lattice QCD*, *Nature* **593** (2021) 51–55, [[2002.12347](#)].

- [19] M. Cè et al., *Window observable for the hadronic vacuum polarization contribution to the muon $g-2$ from lattice QCD*, *Phys. Rev. D* **106** (2022) 114502, [[2206.06582](#)].
- [20] EXTENDED TWISTED MASS collaboration, C. Alexandrou et al., *Lattice calculation of the short and intermediate time-distance hadronic vacuum polarization contributions to the muon magnetic moment using twisted-mass fermions*, *Phys. Rev. D* **107** (2023) 074506, [[2206.15084](#)].
- [21] FERMILAB LATTICE, HPQCD, MILC collaboration, A. Bazavov et al., *Light-quark connected intermediate-window contributions to the muon $g-2$ hadronic vacuum polarization from lattice QCD*, *Phys. Rev. D* **107** (2023) 114514, [[2301.08274](#)].
- [22] N. Chakrabarty, D. K. Ghosh, B. Mukhopadhyaya and I. Saha, *Dark matter, neutrino masses and high scale validity of an inert Higgs doublet model*, *Phys. Rev. D* **92** (2015) 015002, [[1501.03700](#)].
- [23] D. K. Ghosh, N. Ghosh, I. Saha and A. Shaw, *Revisiting the high-scale validity of the type II seesaw model with novel LHC signature*, *Phys. Rev. D* **97** (2018) 115022, [[1711.06062](#)].
- [24] S. Bhattacharya, P. Ghosh, A. K. Saha and A. Sil, *Two component dark matter with inert Higgs doublet: neutrino mass, high scale validity and collider searches*, *JHEP* **03** (2020) 090, [[1905.12583](#)].
- [25] J. Bernon, J. F. Gunion, H. E. Haber, Y. Jiang and S. Kraml, *Scrutinizing the alignment limit in two-Higgs-doublet models: $m_h=125$ GeV*, *Phys. Rev. D* **92** (2015) 075004, [[1507.00933](#)].
- [26] J. Bernon, J. F. Gunion, H. E. Haber, Y. Jiang and S. Kraml, *Scrutinizing the alignment limit in two-Higgs-doublet models. II. $m_H=125$ GeV*, *Phys. Rev. D* **93** (2016) 035027, [[1511.03682](#)].
- [27] A. Crivellin, A. Kokulu and C. Greub, *Flavor-phenomenology of two-Higgs-doublet models with generic Yukawa structure*, *Phys. Rev.* **D87** (2013) 094031, [[1303.5877](#)].
- [28] A. Arbey, F. Mahmoudi, O. Stal and T. Stefaniak, *Status of the Charged Higgs Boson in Two Higgs Doublet Models*, *Eur. Phys. J.* **C78** (2018) 182, [[1706.07414](#)].
- [29] M. Hussain, M. Usman, M. A. Paracha and M. J. Aslam, *Constraints on Two Higgs Doublet Model Parameters in the light of rare B-Decays*, *Phys. Rev.* **D95** (2017) 075009, [[1703.10845](#)].
- [30] N. G. Deshpande and E. Ma, *Pattern of Symmetry Breaking with Two Higgs Doublets*, *Phys. Rev.* **D18** (1978) 2574.
- [31] S. Nie and M. Sher, *Vacuum stability bounds in the two Higgs doublet model*, *Phys. Lett.* **B449** (1999) 89–92, [[hep-ph/9811234](#)].
- [32] J. F. Gunion and H. E. Haber, *The CP conserving two Higgs doublet model: The Approach to the decoupling limit*, *Phys. Rev.* **D67** (2003) 075019, [[hep-ph/0207010](#)].
- [33] A. Arhrib, *Unitarity constraints on scalar parameters of the standard and two Higgs doublets model*, in *Workshop on Noncommutative Geometry, Superstrings and Particle Physics*, 12, 2000, [[hep-ph/0012353](#)].
- [34] S. Kanemura, T. Kubota and E. Takasugi, *Lee-Quigg-Thacker bounds for Higgs boson masses in a two doublet model*, *Phys. Lett. B* **313** (1993) 155–160, [[hep-ph/9303263](#)].

- [35] D. A. Dicus and V. S. Mathur, *Upper bounds on the values of masses in unified gauge theories*, *Phys. Rev.* **D7** (1973) 3111–3114.
- [36] B. W. Lee, C. Quigg and H. B. Thacker, *The Strength of Weak Interactions at Very High-Energies and the Higgs Boson Mass*, *Phys. Rev. Lett.* **38** (1977) 883–885.
- [37] B. W. Lee, C. Quigg and H. B. Thacker, *Weak Interactions at Very High-Energies: The Role of the Higgs Boson Mass*, *Phys. Rev. D* **16** (1977) 1519.
- [38] I. F. Ginzburg and I. P. Ivanov, *Tree-level unitarity constraints in the most general 2HDM*, *Phys. Rev. D* **72** (2005) 115010, [[hep-ph/0508020](#)].
- [39] GFITTER collaboration, M. Baak, *Review of electroweak fits of the SM and beyond, after the Higgs discovery – with Gfitter*, *PoS EPS-HEP2013* (2013) 203.
- [40] L. Lavoura and L.-F. Li, *Making the small oblique parameters large*, *Phys. Rev.* **D49** (1994) 1409–1416, [[hep-ph/9309262](#)].
- [41] M. Baak, M. Goebel, J. Haller, A. Hoecker, D. Kennedy, R. Kogler et al., *The Electroweak Fit of the Standard Model after the Discovery of a New Boson at the LHC*, *Eur. Phys. J.* **C72** (2012) 2205, [[1209.2716](#)].
- [42] A. Broggio, E. J. Chun, M. Passera, K. M. Patel and S. K. Vempati, *Limiting two-Higgs-doublet models*, *JHEP* **11** (2014) 058, [[1409.3199](#)].
- [43] J. Haller, A. Hoecker, R. Kogler, K. Mönig, T. Peiffer and J. Stelzer, *Update of the global electroweak fit and constraints on two-Higgs-doublet models*, *Eur. Phys. J.* **C78** (2018) 675, [[1803.01853](#)].
- [44] H.-J. He, N. Polonsky and S.-f. Su, *Extra families, Higgs spectrum and oblique corrections*, *Phys. Rev. D* **64** (2001) 053004, [[hep-ph/0102144](#)].
- [45] W. Grimus, L. Lavoura, O. M. Ogreid and P. Osland, *A Precision constraint on multi-Higgs-doublet models*, *J. Phys. G* **35** (2008) 075001, [[0711.4022](#)].
- [46] G. Bhattacharyya and D. Das, *Scalar sector of two-Higgs-doublet models: A minireview*, *Pramana* **87** (2016) 40, [[1507.06424](#)].
- [47] ATLAS, CMS collaboration, G. Aad et al., *Measurements of the Higgs boson production and decay rates and constraints on its couplings from a combined ATLAS and CMS analysis of the LHC pp collision data at $\sqrt{s} = 7$ and 8 TeV*, *JHEP* **08** (2016) 045, [[1606.02266](#)].
- [48] CMS collaboration, A. M. Sirunyan et al., *Combined measurements of Higgs boson couplings in proton–proton collisions at $\sqrt{s} = 13$ TeV*, *Eur. Phys. J. C* **79** (2019) 421, [[1809.10733](#)].
- [49] ATLAS collaboration, G. Aad et al., *Combined measurements of Higgs boson production and decay using up to 80 fb⁻¹ of proton-proton collision data at $\sqrt{s} = 13$ TeV collected with the ATLAS experiment*, *Phys. Rev. D* **101** (2020) 012002, [[1909.02845](#)].
- [50] CMS collaboration, V. Khachatryan et al., *Search for neutral MSSM Higgs bosons decaying into a pair of bottom quarks*, *JHEP* **11** (2015) 071, [[1506.08329](#)].
- [51] CMS collaboration, C. Collaboration, *Search for a narrow heavy decaying to bottom quark pairs in the 13 TeV data sample*, *CMS-PAS-HIG-16-025*, .
- [52] CMS collaboration, V. Khachatryan et al., *Search for heavy resonances decaying to two Higgs bosons in final states containing four b quarks*, *Eur. Phys. J. C* **76** (2016) 371, [[1602.08762](#)].

- [53] CMS collaboration, A. M. Sirunyan et al., *Search for a massive resonance decaying to a pair of Higgs bosons in the four b quark final state in proton-proton collisions at $\sqrt{s} = 13$ TeV*, *Phys. Lett. B* **781** (2018) 244–269, [[1710.04960](#)].
- [54] ALEPH, DELPHI, L3, OPAL, LEP collaboration, G. Abbiendi et al., *Search for Charged Higgs bosons: Combined Results Using LEP Data*, *Eur. Phys. J. C* **73** (2013) 2463, [[1301.6065](#)].
- [55] A. Crivellin, D. Müller and C. Wiegand, *$b \rightarrow s\ell^+\ell^-$ transitions in two-Higgs-doublet models*, *JHEP* **06** (2019) 119, [[1903.10440](#)].
- [56] P. Bechtle, S. Heinemeyer, O. Stål, T. Stefaniak and G. Weiglein, *HiggsSignals: Confronting arbitrary Higgs sectors with measurements at the Tevatron and the LHC*, *Eur. Phys. J. C* **74** (2014) 2711, [[1305.1933](#)].
- [57] O. Stål and T. Stefaniak, *Constraining extended Higgs sectors with HiggsSignals*, *PoS EPS-HEP2013* (2013) 314, [[1310.4039](#)].
- [58] P. Bechtle, S. Heinemeyer, O. Stål, T. Stefaniak and G. Weiglein, *Probing the Standard Model with Higgs signal rates from the Tevatron, the LHC and a future ILC*, *JHEP* **11** (2014) 039, [[1403.1582](#)].
- [59] P. Bechtle, S. Heinemeyer, T. Klingl, T. Stefaniak, G. Weiglein and J. Wittbrodt, *HiggsSignals-2: Probing new physics with precision Higgs measurements in the LHC 13 TeV era*, *Eur. Phys. J. C* **81** (2021) 145, [[2012.09197](#)].
- [60] H. Bahl, T. Biekötter, S. Heinemeyer, C. Li, S. Paasch, G. Weiglein et al., *HiggsTools: BSM scalar phenomenology with new versions of HiggsBounds and HiggsSignals*, *Comput. Phys. Commun.* **291** (2023) 108803, [[2210.09332](#)].
- [61] P. Bechtle, O. Brein, S. Heinemeyer, G. Weiglein and K. E. Williams, *HiggsBounds: Confronting Arbitrary Higgs Sectors with Exclusion Bounds from LEP and the Tevatron*, *Comput. Phys. Commun.* **181** (2010) 138–167, [[0811.4169](#)].
- [62] P. Bechtle, O. Brein, S. Heinemeyer, G. Weiglein and K. E. Williams, *HiggsBounds 2.0.0: Confronting Neutral and Charged Higgs Sector Predictions with Exclusion Bounds from LEP and the Tevatron*, *Comput. Phys. Commun.* **182** (2011) 2605–2631, [[1102.1898](#)].
- [63] P. Bechtle, O. Brein, S. Heinemeyer, O. Stal, T. Stefaniak, G. Weiglein et al., *Recent Developments in HiggsBounds and a Preview of HiggsSignals*, *PoS CHARGED2012* (2012) 024, [[1301.2345](#)].
- [64] P. Bechtle, O. Brein, S. Heinemeyer, O. Stål, T. Stefaniak, G. Weiglein et al., *HiggsBounds – 4: Improved Tests of Extended Higgs Sectors against Exclusion Bounds from LEP, the Tevatron and the LHC*, *Eur. Phys. J. C* **74** (2014) 2693, [[1311.0055](#)].
- [65] P. Bechtle, S. Heinemeyer, O. Stal, T. Stefaniak and G. Weiglein, *Applying Exclusion Likelihoods from LHC Searches to Extended Higgs Sectors*, *Eur. Phys. J. C* **75** (2015) 421, [[1507.06706](#)].
- [66] P. Bechtle, D. Dercks, S. Heinemeyer, T. Klingl, T. Stefaniak, G. Weiglein et al., *HiggsBounds-5: Testing Higgs Sectors in the LHC 13 TeV Era*, *Eur. Phys. J. C* **80** (2020) 1211, [[2006.06007](#)].
- [67] H. Bahl, V. M. Lozano, T. Stefaniak and J. Wittbrodt, *Testing exotic scalars with HiggsBounds*, *Eur. Phys. J. C* **82** (2022) 584, [[2109.10366](#)].

- [68] LZ collaboration, J. Aalbers et al., *First Dark Matter Search Results from the LUX-ZEPLIN (LZ) Experiment*, *Phys. Rev. Lett.* **131** (2023) 041002, [[2207.03764](#)].
- [69] FERMI-LAT collaboration, M. Ackermann et al., *Searching for Dark Matter Annihilation from Milky Way Dwarf Spheroidal Galaxies with Six Years of Fermi Large Area Telescope Data*, *Phys. Rev. Lett.* **115** (2015) 231301, [[1503.02641](#)].
- [70] D. Chowdhury and O. Eberhardt, *Global fits of the two-loop renormalized Two-Higgs-Doublet model with soft Z_2 breaking*, *JHEP* **11** (2015) 052, [[1503.08216](#)].
- [71] F. Staub, *From Superpotential to Model Files for FeynArts and CalcHep/CompHep*, *Comput. Phys. Commun.* **181** (2010) 1077–1086, [[0909.2863](#)].
- [72] F. Staub, *Automatic Calculation of supersymmetric Renormalization Group Equations and Self Energies*, *Comput. Phys. Commun.* **182** (2011) 808–833, [[1002.0840](#)].
- [73] F. Staub, *SARAH 3.2: Dirac Gauginos, UFO output, and more*, *Comput. Phys. Commun.* **184** (2013) 1792–1809, [[1207.0906](#)].
- [74] F. Staub, *Exploring new models in all detail with SARAH*, *Adv. High Energy Phys.* **2015** (2015) 840780, [[1503.04200](#)].
- [75] J. Oredsson, *2HDME : Two-Higgs-Doublet Model Evolver*, *Comput. Phys. Commun.* **244** (2019) 409–426, [[1811.08215](#)].
- [76] XENON collaboration, E. Aprile et al., *Projected WIMP sensitivity of the XENONnT dark matter experiment*, *JCAP* **11** (2020) 031, [[2007.08796](#)].
- [77] XENON collaboration, E. Aprile et al., *Search for New Physics in Electronic Recoil Data from XENONnT*, *Phys. Rev. Lett.* **129** (2022) 161805, [[2207.11330](#)].
- [78] PANDAX-II collaboration, C. Cheng et al., *Search for Light Dark Matter-Electron Scatterings in the PandaX-II Experiment*, *Phys. Rev. Lett.* **126** (2021) 211803, [[2101.07479](#)].
- [79] PANDAX-4T collaboration, Y. Meng et al., *Dark Matter Search Results from the PandaX-4T Commissioning Run*, *Phys. Rev. Lett.* **127** (2021) 261802, [[2107.13438](#)].
- [80] N. D. Christensen and C. Duhr, *FeynRules - Feynman rules made easy*, *Comput. Phys. Commun.* **180** (2009) 1614–1641, [[0806.4194](#)].
- [81] G. Belanger, F. Boudjema, A. Pukhov and A. Semenov, *micrOMEGAs_3: A program for calculating dark matter observables*, *Comput. Phys. Commun.* **185** (2014) 960–985, [[1305.0237](#)].
- [82] CMS collaboration, A. M. Sirunyan et al., *Search for invisible decays of a Higgs boson produced through vector boson fusion in proton-proton collisions at $\sqrt{s} = 13$ TeV*, *Phys. Lett. B* **793** (2019) 520–551, [[1809.05937](#)].